Spring 5-6-2022

Assessment of Cellular Alignment and Proliferation on Cellulose Nanofibril(CNF) Films

Sahar Roozbahani
University of Maine, sahar.roozbahani@maine.edu

ASSESSMENT OF CELLULAR ALIGNMENT AND PROLIFERATION ON CELLULOSE NANOFIBRIL(CNF) FILMS

By

Sahar Roozbahani

B.A. Shiraz University College, 2014

M.S. University of Tehran, 2017

A DISSERTATION

Submitted in Partial Fulfillment of the

Requirements for the Degree of

Doctor of Philosophy

(in Biomedical Engineering)

The Graduate School

The University of Maine

May 2022

Advisory Committee:

Michael Mason, Professor of Chemical and Biomedical Engineering, Advisor

Karissa Tilbury, Assistant Professor of Chemical and Biomedical Engineering

David Neivandt, Professor of Chemical and Biomedical Engineering

Mehdi Tajvidi, Associate Professor of Renewable Nanomaterials

Tod O'Brien, DPM

ASSESMENT OF CELLULAR ALIGNMENT AND PROLIFERATION ON CELLULOSE NANOFIBRIL(CNF) FILMS

By Sahar Roozbahani

Dissertation Advisor and Co Advisor: Michael Mason and Karissa Tilbury

An Abstract of the Thesis/Dissertation Presented
in Partial Fulfillment of the Requirements for the
Degree of Doctor of Philosophy
(in Biomedical Engineering)
May 2022

Research on novel biomaterials to address current limitations associated with bone grafting is currently of high demand. Current treatment options for bone regeneration are facing challenges such as donor site morbidity and limited availability, immune rejection, and disease transmission. Research conducted on natural polymers to mimic Extracellular matrix (ECM)structure of bone tissue demonstrated their strong potential to spur bone regeneration. Engineered scaffolds that are inspired by oriented collagen/Hydroxyapatite (HA)structure in natural bone are promising biomaterials that can provide an ECM like structure for primitive mesenchymal cells to grow and differentiate to the bone cells. Cellulose nanofibril (CNF) is a natural and biocompatible polymer that is widely used in tissue engineering and wound healing. CNF has the same size features of collagen and due to its biocompatibility and anisotropy is a potential candidate to recapitulate bone microstructure. Hydroxyapatite (HA) is the major mineral compound of the bone which improves bioactivity and tissue integration attributes of implanted biomaterials. Current study suggests a methodology to induce fiber alignment in CNF/HA nanocomposites and evaluates the potential of oriented CNF/HA nanocomposite material to support cell growth and redirect pre osteoblasts as precursors to osteocytes. This study lays the foundation for the development of synthetic bone mimic scaffolds with affordable cost and relatively simple method

DEDICATION

To all the international students who miss their family every day.

ACKNOWLEDGEMENTS

TABLE OF CONTENTS

LIST OF FIGURES

LIST OF TABLES

x

CHAPTER 1

AN INTRODUCTION TO BONE REGENERATION

1.Introduction

Bone grafting is among the most performed procedures in several therapeutic areas including but not limited to Orthopedics, Traumatology, and Oral surgery. The goal of this approach is to develop new bone tissues at the area of injury like skeletal deficiency or atrophy area. Each year, approximately half a million patients need bone grafting procedures, in US. The estimated costs associated with bone fractures and orthobiologics are at $4.7 billion[1]. The global financial burden of bone repair is estimated to be around $17 billion per year[2]

`   Osteoinduction is defined as a phenomenon that induces osteogenesis during the bone healing process and osteoinduction means cellular differentiation towards bone tissue due to the physicochemical effect or contact with another tissue. The methods used in bone repair interventions are categorized into following groups: autografts, allografts, xenografts, and artificial scaffolds. Given their favorable osteoinductive and osteoinductive attributes, the Autograft is labeled as gold standard treatment , however, it faces challenges like donor-site morbidity and limited availability [3, 4] While allografts and xenografts do not have autograft's limitations, they are susceptible to trigger immune response and disease transmission. Additionally, their osteoinductive properties is frequently weakened by disruptive processing [3, 5] . Each of these treatment options and their drawbacks are further discussed in section 1.3 in this chapter.

Despite the fact that a significant number of bone grafts and substitutes are available, the effective reconstructive treatment entails several challenges. The major challenges include scalability, high cost of production and safety issues related to biological substances[6, 7].

Bone Tissue Engineering (BTE) science works towards addressing challenges by optimizing material engineering and biological science resources with the goal of improving bone regeneration. Bone engineering looks to find inspiration from bone structure, fracture healing process, and bone's natural formation process during the embryonic development phase. Materials like polymer, ceramics, or combination of them are considered as critical components in most of the BTE strategies. These materials offer application flexibility and could be applied in several forms, for example, membranes and 3D scaffolds. These structures are being referred as extracellular matrix(ECM) mimic, meaning that they help with cell attachment, proliferation, and differentiation by serving as mechanical support and creating favorable environment for cells[8]. There are two ways for cells inclusion in the system: Seeding cells onto the material system before implementation or utilizing the cells from surrounding tissues after in-vivo implementation[9].

While inclusion of biological components like growth factors are deemed beneficial, there are several cost and regulatory challenges in place that limits the use of biologics in bone-tissue engineering [9] Clinical translation and commercialization strategies appreciate the materials-only approaches that employs body's own cells to help with bone regeneration and exclude biological factors [5, 10-12]. During bone regeneration process, an oriented ECM is crucial to regulate cell response while maintaining the mechanical support for cells to grow and proliferate[13]. Previous studies have shown that the aligned nanofibers can effectively promote osteoblasts proliferation and migration resulting in better tissue regenaeration performance compated to random structures [14-17]. Given the potential of aligned ECM mimics to spur bone regeneration, characterizing cellular morphology and proliferation on this type of biomaterials is crucial. Current biomaterial solutions for bone regeneration lack the desired characteristics to replace autologous. Therefore, next generation of bone regenerative biomaterials should include engineered ECM mimics that replicate aligned nanostructure of natural bone while possessing bioactivity for tissue integration. Given the rising interest in using natural polymers such as nanocellulose with

distinguished properties for bone regeneration[18, 19], current study evaluates the potential of aligned cellulose nanofibril (CNF) composites to support cellular alignment and proliferation.

1.1. Bone microstructure

Bone is a composite material in which its core components are matrices of collagen fibrils associated with approximately equal volumes of minerals, where calcium phosphate is the dominant solid mineral phase[20, 21]. The mature mineral matrix is a cross-fibrillar mineralization that originates at the nanoscale where organized layers of mineral units align and span laterally across adjacent collagen fibrils[20].This cross-fibrillar mineralization structure contributes to the structural integrity of bone which relates to how the mineral composition can affect chemical and physical properties, such as density, hardness, and growth morphology[22, 23]. Bone mineral is known to possess compositional and structural similarities with synthetic stoichiometric hydroxyapatite (HA), $Ca_{10}(PO_4)_6(OH)_2$. However, bone mineral is structurally disordered and compositionally nonstoichiometric due to the presence of a substantial amount of anionic and cationic species, as well as ion vacancies in the crystal lattice[24]. The low degree of crystallinity and small crystal size are closely related to the higher solubility of biological apatite compared to stoichiometric hydroxyapatite (HA).

A schematic of bone hierarchical structure is represented in Figure 1.1. At nanoscale, collagen and HA form the backbone of Lamela structure. This oriented matrix maintains the structural stability of the bone tissue and regulates cells response. Engineered biomaterials intended to be used for bone regeneration need to maintain an oriented matrix that induces proper cellular function including adhesion, orientation, proliferation, and differentiation[25-27].
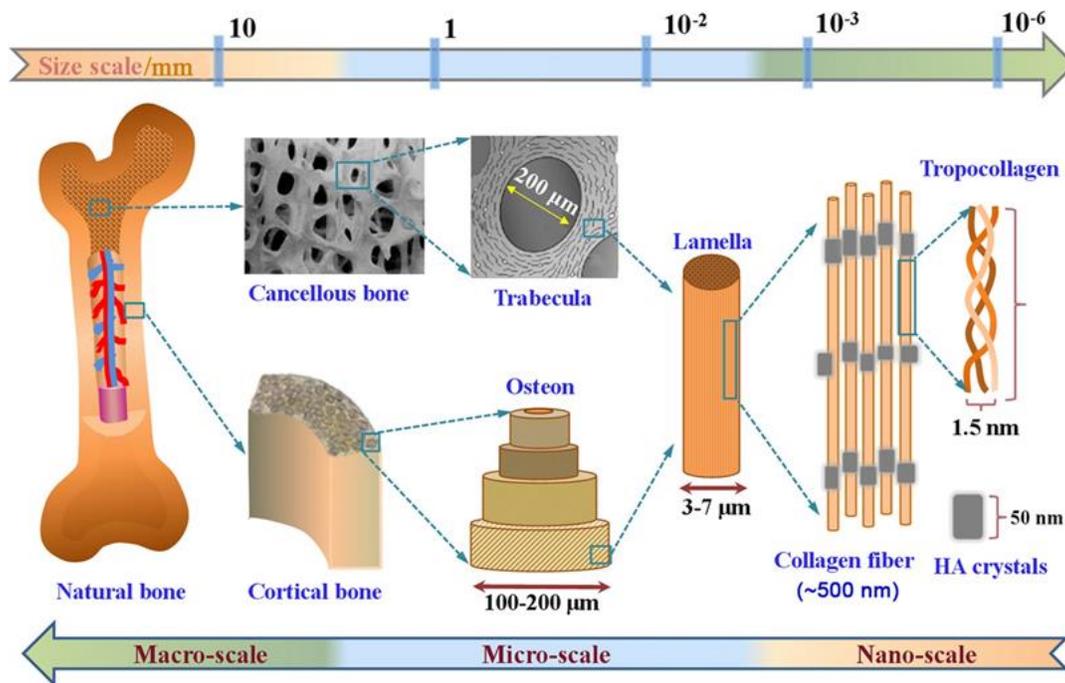
Figure 1. 1representative image bone microenvironment [20]

1.4. Bone defects

Bone regeneration is a complex physiological process of bone formation involving coordinated work by several cell types which can be observed during normal fracture healing, as well as during skeletal development and continuous remodeling throughout adult life[28, 29]. In the case of injury, bone heals by generating new bone being eventually indistinguishable from the adjacent uninjured bone[30].

Fracture healing is assumed to happen in chronological order. Although categorizing healing mechanism into different stages is beneficial to understand underlying biology, however these phases occur simultaneously in multiple sites and at different rates throughout the fractured callus[31]. These phases include hematoma formation and inflammatory response, proliferation/differentiation, matrix ossification and remodeling phase.

The success of bone regeneration relies on the biological and mechanical environment. There are cases of fracture healing in which bone regeneration is impaired. Individual risk factors that can also contribute

to failure of bone regeneration include but not limited to age, diabetes and peripheral vascular disease[32].

At the final stage of bone regeneration, woven bone is deposited on the cartilage callus. A disruption in angiogenesis at this stage can produce a non-healing bone, which is typically referred to as a delayed union or non-union[33]. One study observed 41 trauma centers with 416 patients being treated for tibial shaft fractures. The results showed 13% of fractures occurring in the tibia being associated with delayed union or fracture non-union. Studies suggest that the severity of soft tissue injury is the most important factor determining bone healing[34]. Additionally, other circumstances in orthopedic, oral, and maxillofacial surgery require bone regeneration in large quantities, making it difficult for individuals to self-heal. Some examples include skeletal reconstruction of large bone defects created by trauma, infection, tumor resection, skeletal abnormalities, or cases in which the regenerative process is compromised, including avascular necrosis and osteoporosis[32].

1.4. **Bone grafting**

There is a variety of treatment options available for bone regeneration to replace, restore, or help manage many of these complex clinical situations. The "Diamond Concept" of Peter Giannoudis argues that there are four known factors contributing to bone restoration that should be provided equal acknowledgement; those factors include growth factors, osteoconductive scaffolds, mesenchymal stem cells, and the mechanical environment[35]. The autologous bone graft is the most reliable method to induce bone regeneration[3], However, concerns and limitations include the lack of sufficient transplantable materials, donor site morbidity, inflammation, and resorption of the implanted bone[5, 36]. Alternative options such as the use of allografts or synthetic grafting materials address these limitations, but these alternatives are also limited by immunogenic responses or lack of osteoinductivity [36].

Allogeneic bone is available in a variety of shapes including demineralized bone matrix (DBM), morselized and cancellous chips, corticocancellous and cortical grafts, and whole-bone segments, depending on the needs of the patient. Each of the grafting materials' biological properties vary, but overall, they lack in osteoinductive properties and do not have any cellular components because donor grafts are devitalized through gamma-irradiation or freeze-drying processing which weakens the mechanical properties of the bone and deactivates proteins that are normally found in healthy bones[37, 38]. There are issues of immunogenicity and rejection reactions, possibility of infection transmission, laborious procedure, mechanical resistance, weak osteoinductive and osteogenic properties, and cost[37, 39]. Xenograft bone substitutes originate from a species that is different from that of the recipient which can be freeze-dried or demineralized and deproteinized.

Xenografts are typically only used as a calcified matrix and have been more successful in dentistry than in orthopedics. It also has the risk of disease transmission and is non osteoinductive[38, 39]. Previously mentioned drawbacks of these grafting methods have prompted the development of synthetic bone substitutes.

Table 1.1. Advantages and limitations of grafting methods

Type	Advantages	Drawbacks
Autograft	- Osteogenesis - Osteoinductive: - Osteoconductive - Lack of immune response - No disease transmission	- Donor site morbidity due to harvesting - Limited donor site: limited amount - Multiple incisions
Allograft	- Osteoinductive, - Osteoconductive - No second surgical site	- No osteogenesis - Disease transmission - Dependent on donor's bone state such as age
Xenograft	- No morbidity of donor site - Unlimited amount - Osteoconductive	- No osteoinduction - Disease transmission - Non-resorbable in vivo

1.4. Bone Scaffolds

Ideally a bone graft, scaffold, or substitute should provide similar osteoconductive and osteogenic properties as autogenous bone[40]. The scaffold is an engineered structure that aims to provide mechanical and physiological support to cells for *in vitro* tissue regeneration and *in vivo* implantation. It is vital that the micro and macro structures of the scaffold are designed properly and hold their position because their form directly affects the adhesion and differentiation of cells[41, 42]. In order to overcome the limitations of three grafting methods summarized in Table 1.1, a variety of biocompatible materials have been used. This includes natural polymers such as alginate, collagen, synthetic polymers such as polycaprolactone (PCL) and poly lactic-co-glycolic acid; as well as bio-ceramics such as hydroxyapatite and calcium phosphate[40, 41]. Although these substitutes are effective to some extent, however, limitations such as lack of bioactivity, low cell affinity, brittleness and hydrophobicity restrict their applications. Table1.2 summarizes the advantage and limitations of biomaterials used for bone grafting.

Table1. 2. Advantages and disadvantages of current biomaterials used for bone grafting

Biomaterial	Advantage	Drawback
Natural polymers Collagen	Similar to ECM Cytocompatibility Enzymatic biodegradability FDA approved	Low mechanical strength Low thermal and chemical stability Difficult disinfection Difficult handling
Chitosan	Cytocompatibility Biodegradability Cell-binding, differentiation, and migration properties Antibacterial properties Mucoadhesive Easy properties tunability	Poor mechanical strength and stability Rapid in vivo degradation rate

Table1. 2 Continued

Alginate	Cytocompatibility Cytocompatibility Tunable properties Easy gelling	Difficult to sterilize Low cell adhesion
Cellulose	Hydrophilicity Cytocompatibility Bioactivity Mechanical strength Tunable properties Thermal stability	Limited number of *in vivo* studied to assess degradation
Synthetic polymers Poly lactic acid (PCL)	Cytocompatibility Biodegradability Slow degradation rate	-Inflammatory caused by acid degradation products; Limited mechanical property; Slow biodegradability -Degrade too fast, Mild cytotoxicity
Poly Lactic Acid (PLA)	Cytocompatibility Biodegradability Slow degradation rate	Hydrophobicity Low bioactivity
Poly lactic co glycolic Acid(PLGA)	Wide range of degradation rate Tunability	Suboptimal mechanical properties Poor osteoconductivity
Bioceramics Calcium Phosphates (HA, β-TCP) Bioactive glass	- biocompatibility; Supporting cell activity; Good osteoconductivity - biocompatibility; Supporting cell activity; osteoconductive; Vascularization; Rapid gene expression; Tailorable degradation rate	-Very brittle -No flexibility

Cellulose is the most abundant polymeric material found in nature. It possesses biocompatibility, protein binding sites on its surface, mechanical strength, and anisotropy. In addition, high density of reactive hydroxyl groups on its surface, facilitate the immobilization of cell adhesive proteins[41]. Cellulose nanofiber (CNF) is flexible, degrades in vivo[43] and has size features similar to natural collagen fibrils [44]. Therefore, it has a great potential for tissue engineering[45] and bone regeneration applications. Incorporating bioactive minerals, such as hydroxyapatite into CNF matrix can improve cell adhesion, cell differentiation, and osteoinduction making it a potential candidate for bone regeneration applications[46, 47] .

CHAPTER 2

ONE STEP HYDROTHERMAL SYNTHESIS OF BIOLOGICALY RELEVANT HYDROXYAPATITE

Contribution to the project

The work presented in this chapter is the result of a collaborative project and my contribution include, Hydroxyapatite synthesis, FTIR analysis, SEM analysis, TEM analysis and co authoring the manuscript. Co authors include Mitchel Chesley, Reymond Kennard, Su Min Kim, Kora Kukka and Michael Mason

2.1 Introduction

Up to 70% of natural bone is comprised of hydroxyapatite (HA), which includes several sub-forms with trace metals and ions such as magnesium, carbonate ions, and acid phosphates, collectively described as bone material[48, 49]. Additionally, natural HA has disordered nanostructures[50] that help to improve bioavailability within applications such as bone implants, with relatively small crystalline domain sizes ~20 nm[49, 51] that have been shown to improve the promotion of cell growth[52]. Reportedly, this is in part due to the increased physical interaction between cells and the host material that arises as a result of the large surface-to-volume ratio of the nano-sized particles[53]. Although HA can be extracted from natural sources such as fishbone[54], eggshells[55] and bovine bones[56], these processes can be extremely time consuming and cost-prohibitive.

Synthetic HA (formula of $Ca_5(PO_4)_3OH$), is considered promising bone substitute due to its biocompatibility, osteoconductive and osteoinductive behavior, and ability to create a firm bond with bone tissue[57-61], but typically lacks many of the naturally prevalent ionic substitutions (e.g., F^-, CO_3^{2-}, Na^+, Mg^{2+}, Zn^{2+}, and Sr^{2+}). It has been proposed that synthetic HA material, intended as an implanted scaffolding system, would better promote the *in vivo* growth of mineralized bone with these substitutions[61, 62]. Synthetic HA has been created by different methods such as co-precipitation[63],

sol-gel[64], hydrothermal processing[65] and solid-state reaction methods[66]. Although these methods are effective in creating materials that are chemically analogous to natural HA, they are generally unable to produce HA materials with the desired submicron particle sizes. As such, a post-synthesis particle milling step is frequently applied to yield micron and nanometer-sized powders. Combined, these mechano-chemical methods can take more than 48 hours per batch[67]. In general, cost-efficient forms of synthetic HA with sub-micron particle size demonstrating the metabolic activity, dynamic response to the environment, and the immunogenic response of natural HA[51, 68] are not yet readily available.

In this study, a simple hydrothermal method presented by Liu *et al* [62] was modified to develop an *in situ* one-step synthesis method capable of efficiently producing large quantities of biologically relevant HA suitable for use in biological applications and as a precursor for further modification to create chemically and morphologically biomimetic HA. This method presented here explores the use of an *in-situ* milling process to create mechanical shearing effects on the HA crystallites during synthesis to reduce and refine the size of final particulates. The simple method also avoids the need for continuous monitoring of pH and temperature that is prevalent in other HA synthesis approaches[63, 64, 66]. The resulting elemental stoichiometric ratios, and crystallite and aggregate sizes were compared to commercially available, biologically relevant HA. Fourier Transform Infrared spectroscopy (FT-IR) was used to determine the stoichiometric Ca:P ratios in the resulting powders to verify the production of HA, to determine the optimum reaction time, and to confirm that *in situ* and *ex situ* milling did not adversely affect the chemical composition of the synthesized HA. X-ray powder diffraction (XRD) was used to determine the crystallinity and primary crystallite size of the as-prepared samples. A Malvern Mastersizer along with scanning electron microscopy (SEM) and transmission electron microscopy (TEM) were used to characterize particle morphology, including the extent of aggregation and the size distributions of resulting aggregates.

2.2. HA synthesis

A simplified hydrothermal synthesis method for HA developed by Liu *et al.*[62] was modified for the production of HA in this study. HA was synthesized using a ~200 g total powder mixture, with a 3:7 stoichiometric ratio, of calcium phosphate monobasic to calcium hydroxide, respectively. The mixture was initially placed in the ball mill container along with zirconia milling media, in the ratio of 3:1 milling media to powder, by weight. Samples intended for *ex situ* processing were milled for 1 hour to ensure homogeneous mixing before being placed into the hydrothermal reactor with 2 L of DI water. Five different HA samples were synthesized varying the reaction time from 2-6 hours, in one-hour increments. The temperature was held constant at 109°C similar to a procedure done by Liu *et al.*[62], this was done for all reactions. The high pH (>10) of the resulting concentration of calcium ion of mixture required no other reducing agents for the synthesis of the HA[69]. The resulting solution was left undisturbed for 12 hours allow the reactor to cool and for the HA particulates to settle. The as-synthesized precipitated product was then decanted to remove excess water. The remaining material was washed three times with deionized water to ensure the removal of any unreacted precursors. After washing, the product was oven-dried, in air, at 100°C for 24 hours. The resulting powders were bright white in appearance, and clumpy in nature. BM was again implemented, *ex situ,* here to break apart the larger visible clumps, reduce particulate aggregation, and to refine the particle size distribution. Different milling times were explored and the effect on particle size determined. A simplified process flow diagram for the entire synthesis is presented in Figure 2.1
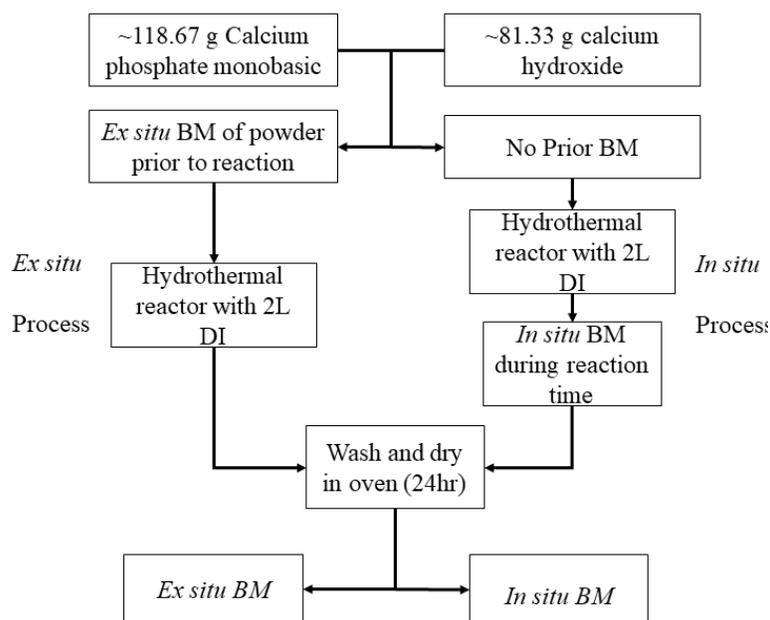
Figure2. 1Process flow diagram for hydrothermal synthesis of

As stoichiometric ratio and (nanoscale) crystalline grain sizes are both critical for biologically relevant HA, synthesis methods that promote homogeneous reactant dispersion are of interest. *In situ* methods involving the use of ultrasonic mixing have previously been implemented and shown to reduce reaction times and promote the production of smaller nano-crystalline particles[70]. This same work, performed by Poinern *et al.*[70], suggests that the use of ultrasound can alter the stoichiometric ratio of the product, which may not be desirable. This was mitigated with the use of high thermal post-treatment temperatures (400°C), which affected nanoparticle shape. In order to avoid these effects, while still producing chemically and morphologically relevant HA, a simple low-cost *in situ* ball-milling method was investigated. This was achieved by securely fastening the hydrothermal reactor system into a fully enclosed Series 25 Incubator Shaker chest, which was operated in an isolated location. The hydrothermal reaction time and shaking frequency were held constant at 4-hours and 200 rpm, respectively. With 4 different *in situ* milling variations; no milling media, 1-inch diameter steel milling media only, 0.5-inch

diameter steel milling media only, and a ~50:50 mix by weight of 1 and 0.5-inch steel milling media. During

the synthesis, pressure within the system was held at 50 kPa. Following the reaction, the vessel was

allowed to cool to room temperature, safely reducing the internal pressure, as indicated by the external

float valve. Residual pressure was relieved using the manual pressure relief valve before opening. The

resulting HA samples were oven dried at 100°C, and coarsely crushed using a ceramic mortar and pestle

to break apart large clumps.

2.3. Characterization of synthetic HA

Diffuse reflectance Fourier Transform Infrared (FT-IR) was used to analyze the chemical

composition of the as-synthesized HA. Here FTIR spectra of each sample were recorded on an FTLA

2000 spectrometer (ABB) using an EasiDrift accessory utilizing a sample to KBr ratio of 20 %w/w *(gain of

1, resolution 4cm^{-1}, 40 scans per spectrum). All diffuse reflectance spectra were converted to absorbance

units the using Kubelka-Munk (K-M) model the resulting spectra were filtered using a Savitzky-Golay

model to reduce the apparent noise fluctuations in the data to ease the comparison of more significant

features between samples. For clarity and ease of comparison each spectrum was baseline corrected,

normalized to the largest peak amplitude, and separated into two spectroscopic regions of interest. To

facilitate the assessment of the chemical quality and biological relevance of the samples, a traceable,

widely accessible HA spectrum was used as a reference and target spectrum throughout this study. This

spectrum, reported by NIST, extracted from synthesized HA, has been shown to be mimetic, with the

exception of the absence of known proteins associated with HA, of naturally occurring bone[69], including

Ox femur[70], and fish bone[56]. Relevant spectral features of biological HA should include contributions

from phosphate, carbonate, and hydroxyl ions. In contrast, typical high purity reagent grade HA, which is

often chosen as a suitable reference, may demonstrate spectral characteristics not representative of HA
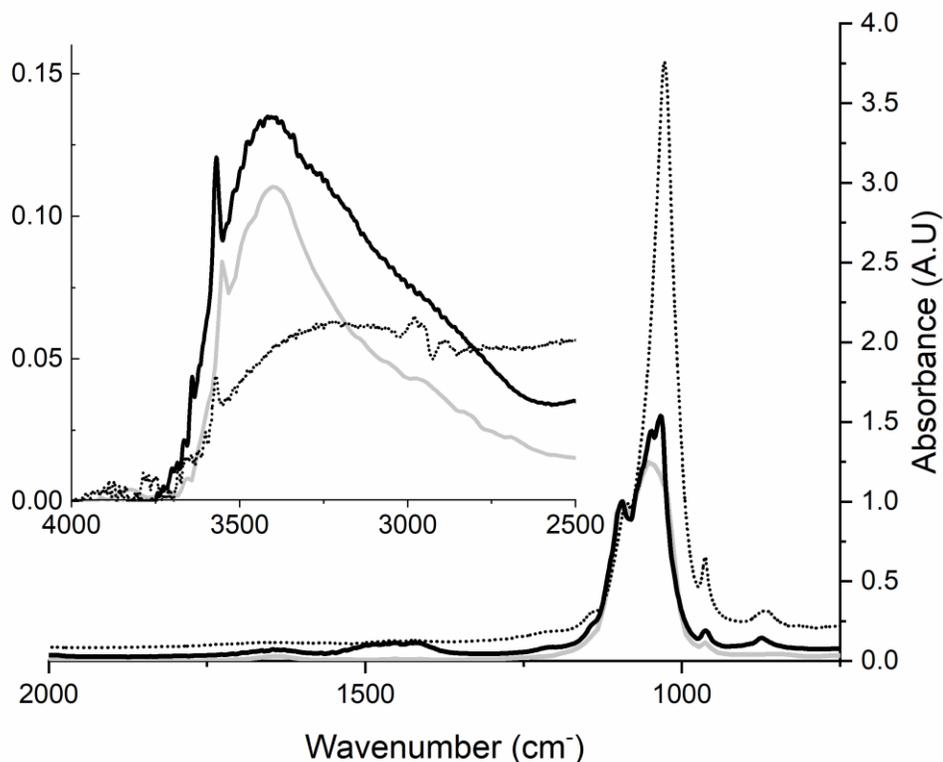
Figure 2. 2. Spectra of hydroxyapatite from three sources, normalized by the 1092 cm-1 phosphate peak following baseline correction. Sigma Aldrich HA (dashed), typical 4hr synthesized HA (black), NIST reported HA (grey).

found in biology. Figure 2.2 shows the comparison of the HA IR spectrum reported by NIST, with the diffuse reflectance IR spectra of both a commercially available HA sample and a typical 4hr HA sample synthesized by the method presented here. The presence of the relatively weak band at 3570 cm^{-1} can be assigned to the primary absorption of OH^- found within the HA lattice. The strongest absorption bands of phosphate are evident at 1092 cm^{-1} and 1030 cm^{-1}, while the primary absorption bands of carbonate appear at 871 cm^{-1} and 1384 cm^{-1}. Weaker carbonate peaks are also visible at 833 cm^{-1} and 1640 cm^{-1}. The CO_3^{2-} peak is known to result from small amounts of carbonated hydroxyapatite which occurs from PO_4^{3-} reacting with CO_2 in the air[66, 71] and is commonly viewed as an impurity in synthetic HA[62, 70]. In fact, as up to 8% of HA found in the naturally occurring bone is in this carbonated form, the presence of some

15

carbonate is desired[49, 59, 63]. The resulting as-synthesized HA powder particle size distributions were initially investigated using a Malvern NanoZS dynamic light scattering instrument. However, due to significant sedimentation effects, results were not reliable. As such a Malvern instruments Mastersizer 2000 (Model: APA2000) was used for size analysis of the dried HA. Particle morphology and possible aggregation was investigated by scanning electron microscopy (SEM) using both an AMRay 1820 and Zeiss NVision 40 Microscope. SEM micrographs were obtained at 500μm and 10μm scale using the AMRay 1820, (10kV, 40X and 1990X, magnification, respectively). Higher resolution SEM micrographs (500nm scale) were acquired at 2kV (20,160X magnification) using the Zeiss NVision 40.

X-ray Diffraction (XRD) was used to assess relative quality as well as identify the crystalline phases present in the as prepared samples. Diffraction data were obtained using a Panalytical Xpert Pro X-ray Diffractometer, with a parabolic mirror and PIXCEL 255 channel solid state detector. A 2θ range of 20-60 was used. Crystalline domain sizes were calculated from the XRD data using the Debye-Scherrer equation. Yields were calculated using the mass of fully dried material (120-180 grams) compared to the total mass of precursor reagents and were between 60 and 80%. The variation in yield was attributed to inconsistency during the wash steps, where some material loss was likely.

2.4. Results and discussion

FT-IR spectra for samples synthesized with reaction times of 2-6 hours, in one-hour increments, were compared to determine the optimum hydrothermal reaction time. According to the previous work by Giraldo-Betancur *et al.*[69]*,* naturally derived HA is chemically distinct from most synthetic forms of HA, having somewhat elevated hydroxyl levels as seen in the OH^- region of Figure 2.2 The desired OH^- contribution, arising specifically from incorporation in the material lattice, is visible as a narrow but relatively weak peak around 3570 cm^{-1}. Separately, a broad OH- contribution resulting from adsorbed

water, except when aggressive drying or calcination methods are employed, is visible around 3375 cm^{-1}. The relative OH$^-$ content can be quantified, for the purpose of optimization of a given sample, as the OH$^-$ / PO$_4^{3-}$ ratio (R). Stoichiometrically, the OH$^-$ content of the material lattice, relative to PO$_4^{3-}$, for idealized HA should be around 1:3 (R = 0.33) , but is expected to be significantly lower when extracted from IR spectra due to the relatively high absorptivity of OH$^-$ relative to PO$_4^{3-}$. This disparity does not affect the utility of IR spectroscopy in identifying optimal parameters or the value of the NIST spectrum as a target for this optimization.

In order to extract a meaningful value for the OH$^-$ / PO$_4^{3-}$ ratio (R), the IR spectra were first background subtracted (linear), and then normalized to primary phosphate peak at ~1092 cm^{-1}, which was the only phosphate peak clearly resolved in all spectra. This normalization highlights differences in both the hydroxyl and phosphate regions of the spectra (Figure2. 2). R values could then be readily determined using the incorporated OH$^-$ peak at 3570 cm^{-1}. A target R-value was determined using the NIST spectrum and is visible as the dashed horizontal line shown in Figure 2.3, having an R-value of 0.08. Extracted R-values for all synthesized samples, as a function of hydrothermal reaction time, are shown in Figure 2. 3. In all cases, the resulting R-values are significantly above that of the target value, with a weak trend indicating that reaction times above 4 hours better approach the target value. Based on this result, and for the sake of process efficiency, further studies were performed using a fixed 4-hour hydrothermal reaction time.
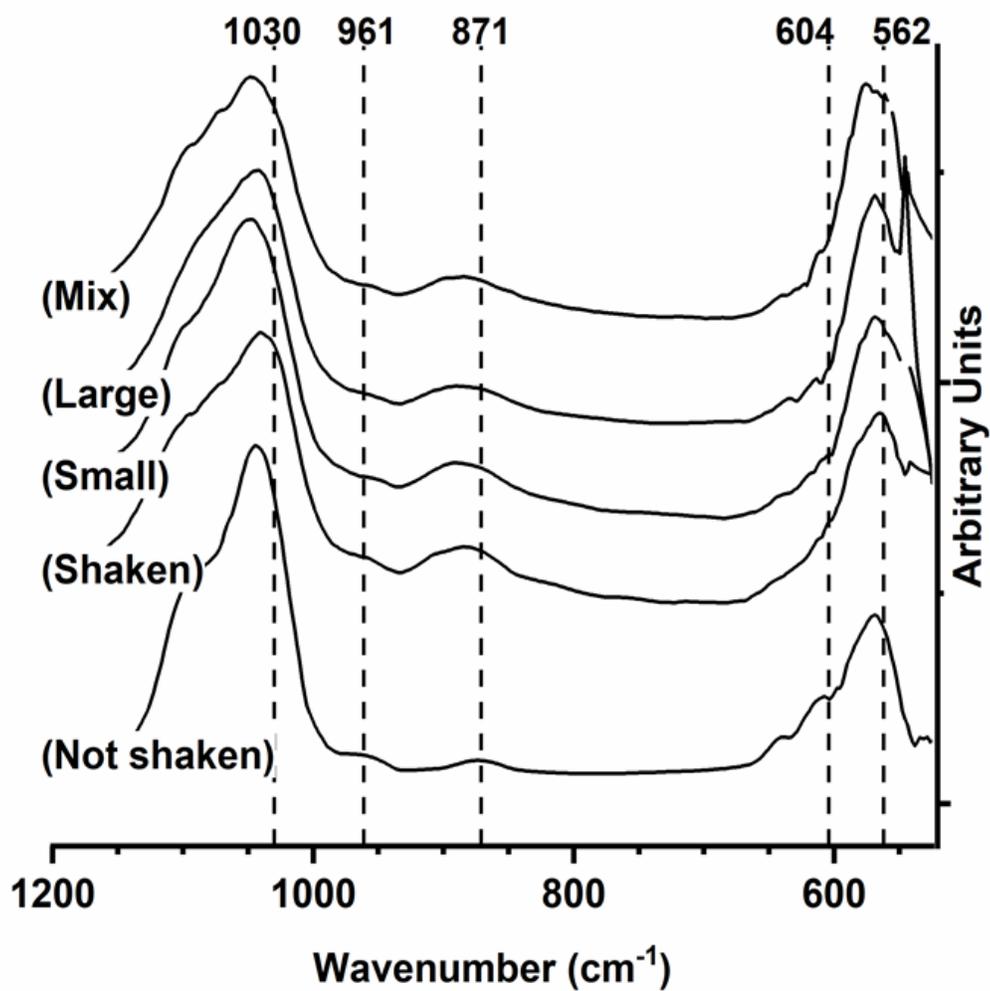
Figure 2. 3. FTIR spectra of hydroxyapatite synthesized with a reaction time of 4 hours. Each of the five samples were prepared under different milling conditions (unmilled, shaken, shaken with small media, shaken with large media, shaken with mixed media). An amplitude offset is used for clarity
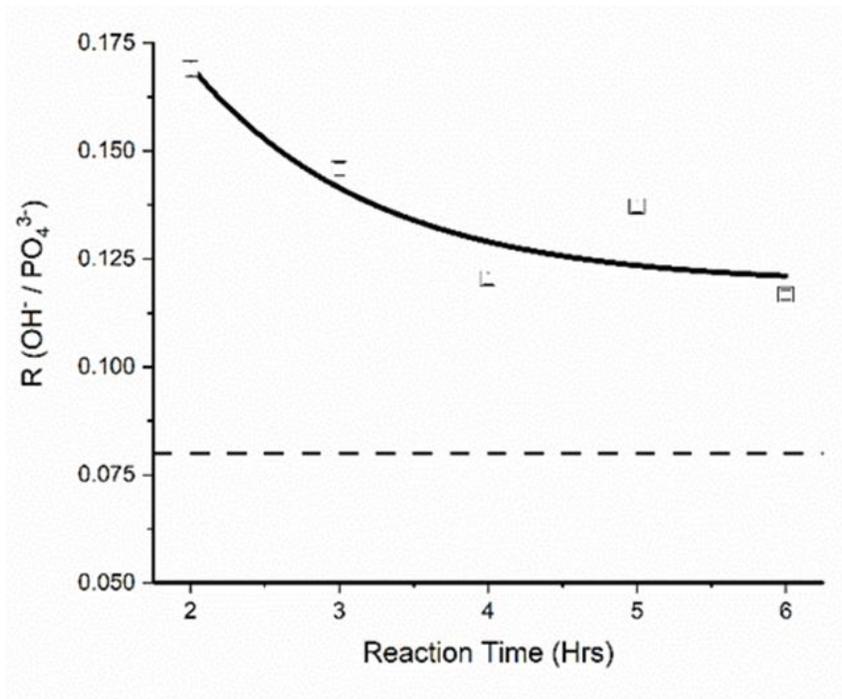
Figure 2. 4. OH- relative to PO43- peak amplitudes vs reaction time. Target value indicated by dashed line. Experimental values, and corresponding variances, are shown as open squares

To investigate the effects of different milling techniques, and to ensure they have no significant effect on chemical composition, several samples using different milling processes were produced, and FT-IR spectra were recorded. Wet and dry milling processes investigated were ex-situ dry ball milling, agitation/shaking during synthesis (as a control), shaking with wet in-situ small steel milling media, shaking with wet in-situ large steel milling media, and shaking with wet in-situ mixture of large and small steel milling media. The resulting spectra are shown in Figure 2.4. Predominant expected peak positions are indicated as vertical dashed lines for ease of comparison. While minor variations between spectra are visible, no significant differences are observed indicating that the use of milling can be explored to affect particle size without adversely altering the chemical composition of the HA. In addition to composition, biologically relevant HA frequently exhibits specific particle and crystalline grain (domain) sizes. As described previously,

accessible crystalline grain sizes on the order of a few tens of nanometers are desirable to promote cell growth. Previous work has reported that crystallinity and grain size are affected by reaction conditions. As such, particle size distributions were obtained for each sample, prepared with different hydrothermal reaction times. The resulting volume weighted size distributions are shown in Figure 2.5. To help quantify the effects of reaction time and milling resulting particle size, the size distributions were divided into three regions of interest, the second region (II) corresponding to the targeted size region (10-100 nm diameter). In general, the particle size distributions of the as-synthesized HA samples all exhibited polydispersity with significant volume fractions between 20 nm and 1000 µm, and multimodal with predominant sub-populations centered around 20 nm and 300 nm. It is immediately evident that the 4 hour reaction time
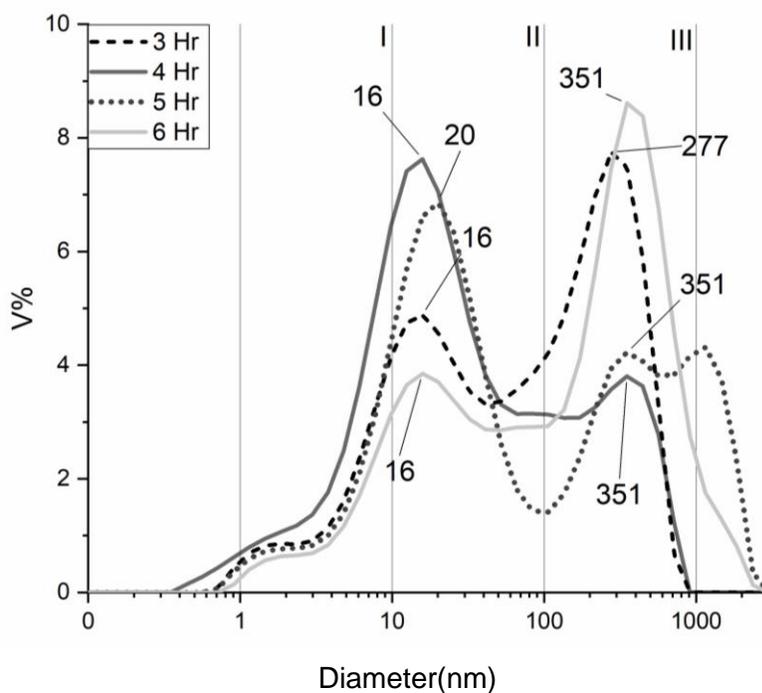
Figure 2. 5. Size distributions of unmilled HA with different hydrothermal reaction times

produces the largest volume fraction of material in the target size region. Interestingly, the targeted volume fraction (region II) increases initially with reaction time, then decreases for longer reaction times. This could be a result of continued crystallite growth, agglomeration, or both.

As it is difficult to distinguish between large individual crystallites and aggregates of smaller crystallites using dry particle sizing, a simple mechanical dry milling post processing step was implemented for each of the as-synthesized samples, in an attempt to break apart aggregates and further increase the volume fraction in the targeted size region. For this, the as-synthesized dried HA (4 hour hydrothermal reaction time) was placed in a ceramic rotary milling apparatus with a ratio of 2:1 zirconia ball media to hydroxyapatite powder, by weight. Dry milling was implemented under ambient conditions for durations ranging from 1 to 24 hours, after which dry particle size distributions were obtained. The volume fractions

Table2. 1. Comparison of size distribution, by size region, for HA with different ex-situ milling times

Reaction (hrs) / Milling (hrs)	Vol% ($\pm1\%$) Region I	Vol% ($\pm1\%$) Region II	Vol% ($\pm1\%$) Region III	Total Vol% Region I-III
4 / 0	25	46	28	99
4 / 1	26	53	19	98
4 / 4	22	57	19	98
4 / 24	21	38	30	89

for each size region were obtained by integrating the size distribution data. The results are shown in Table 2.1.
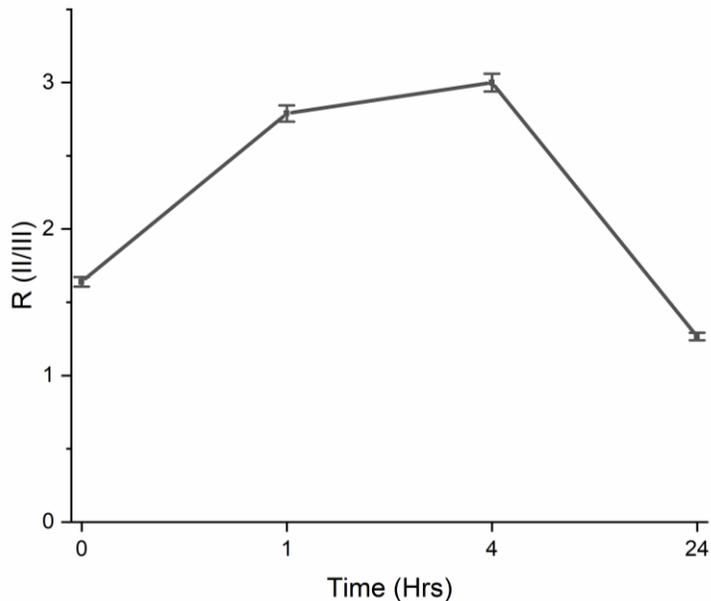
Figure2. 6. Comparison the ratio of the volume fractions of region II, relative to region III (R = Vol% II / Vol% III), as a function of milling duration.

Qualitatively, as the duration of ball milling is increased, the target volume fraction (region II) appears to reach a maximum at four hours. This corresponds to a minimum in the volume fraction of region III. This would seem to suggest that, in fact, the larger particles are either aggregates of smaller particles or are effectively refined by the milling process. This is illustrated in Figure2. 6, where the ratio of the volume fractions of region II, relative to region III (R = Vol% II / Vol% III), are plotted as a function of milling duration. At much longer milling times (24 hours), this ratio is again reduced, suggesting that aggregation of smaller particles is significant, and may be induced by the milling process itself. This is

supported by a similar decrease in the smallest size region (region I) which also shows a decrease in the relative volume fraction at longer milling times.

Based on the limited effect of the dry milling experiments on reducing the contribution of the largest volume fraction, an *in-situ* wet milling approach was developed based on the work of Kotake *et al*[72] This work compared the effects of dry and wet ball milling, including the size and shape distribution of the resulting particles. It is perhaps not surprising that this previous work concluding that wet ball milling conditions produced consistently smaller particle sizes. As such a one-step, one-pot hydrothermal synthesis method, which integrates *in-situ* mixing and milling of HA, was explored.

In this approach, various sized milling media were introduced directly into the hydrothermal reactor which itself was affixed within a shaker chest providing the necessary periodic motion to achieve mechanical milling simultaneous with mixing (shaking). Due to their hardness and anti-corrosion properties, spherical stainless-steel media were used. The reactor was then affixed within a closed shaker table chest to provide simultaneous agitation during 4 hour hydrothermal treatment reaction.

Different combinations of milling media sizes were explored, which included: large (1-inch diameter), small (0.5 inch diameter), and equal parts large/small media (by weight). Following hydrothermal treatment/reaction samples were decanted, washed and oven dried. These samples did not receive additional post reaction *ex-situ* milling. The size distributions for these samples are shown for comparison in Figure 2.7, while the resulting volume fractions, calculated by integrating across each size region, are presented in Table 2.2.
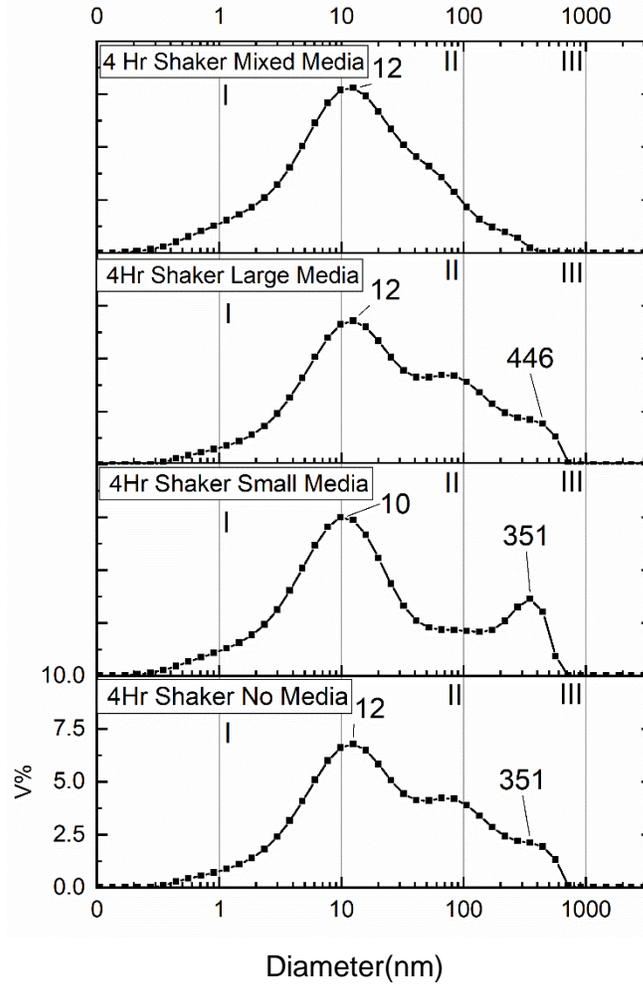
Figure2. 7. Particle size distribution for 4 hours of hydrothermal treatment with simultaneous shaking, with no ball bearings, all large, all small, and 50% small and large milling medium

Table2. 2.Comparison of size distributions, by size region, for 4 hour reaction time with simultaneous shaking and with with varying in-situ milling media

Milling media	Vol% (±1%) Region I	Vol% (±1%) Region II	Vol% (±1%) Region III	Total Vol% Region I-III
no media	32	45	20	98
small media	40	36	20	96
large media	32	45	20	98
large & small media	41	48	7	96

The influence of constant shaking alone, during the 4-hour hydrothermal reaction, on the resultant particle sizes is evidenced by the significant decrease in the largest HA size fraction as compared to HA produced in a fixed reactor followed by ex situ milling (20% and 28%, respectively). When in situ milling is employed simultaneous with shaking, the results are varied. For samples prepared using large milling media, the milling process appears to be largely ineffective, as illustrated by the similarities in the size distributions shown in Figure 2.7 and in the integrated volume fractions of Table 2.2 When only small milling media is used, volume fraction of region I is increased, region II is reduced, and region III remains unchanged. Each of these results is consistent with conventional understanding that larger materials require the use of larger media for effective milling. The largest effect on the size distribution, resulted when equal parts of large and small milling media were used, where the volume fraction of region III decreased by 13%, and both regions I and II increased such that their combined fractions accounted for 90% of the total material volume. In this case the mixed media may act in a kind of stepwise fashion with the large media first breaking apart the larger particles and aggregates, allowing the smaller media to
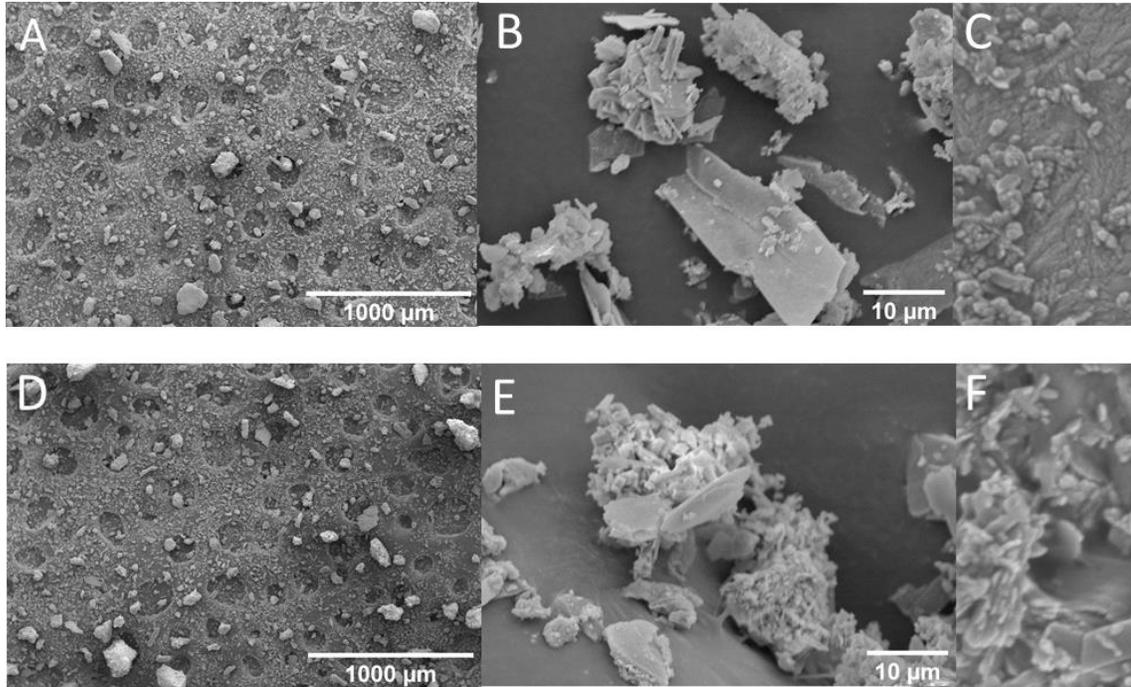
Figure 2. 8. SEM Images of HA particles with increasing magnification, left to right. A-C) 4 hr synthesis, ex situ ball milling only. D-F) 4hr reaction with in situ milling and shaking.

continue the refining process. While prolonged use of mixed media is generally not recommended as it can result in unwanted wear on the (smaller) media, this was not observed possibly due to the relatively short duration of the milling process employed here. Scanning electron microscopy (SEM) was used to help elucidate the makeup of the as produced and milled HA. Specifically, the extent to which the dried as-synthesized HA particles were aggregated, and the varied particle morphologies present were qualitatively investigated. Representative micrographs, across multiple size scales, are shown without modification in Figure 2.8 for unmilled (A, B, C), and *in-situ* milled (mixed media) (D, E, F), HA. The adhesive mounting media used to affix the HA powders is visible as the circular features in the largest area images of Figure2.8 (A and D). In these same images only the largest particles or aggregates are visible and appear similar in size regardless of whether *ex situ* or *in situ* milling was used. When viewed at higher magnification (10 μm scale, Figures 2.8, B and E respectively), some subtle changes in particle size and morphology start to appear. For example, more of the particles in the *in situ* milled materials (Figure2.8E)

26

appear to be smaller, while there appear to be fewer very large particles. The *ex-situ* particles are also more crystalline in appearance. At the highest magnification (Figure2.8, C and F), particles with sizes on the order of tens of nanometers are clearly visible in both sample preparations. While there are qualitative differences in morphology and aggregation visible between the two samples, it is difficult to determine if this is sufficiently representative of the entire sample to warrant any significant conclusions.

TEM micrograph of 4 hour *in situ* shaken HA no BM and mixed BM were taken to as a secondary morphology tool. Samples were sonicated in DI water for ~1 min. TEM images can be seen in Fig 2.9, with 4-hour shaken no BM (A & B) and 4-hour shaken mixed BM (C & D). Due to agglomeration and platelets overlaying one another obtaining focus of the agglomerations was difficult as seen in (Figure 2.9 A & C). With individual particles being seen on the exterior of agglomerates which had better clarity of small platelets. In both images (Figure 2.9 B & D) individual particulates can be seen around 10–30 nm in diameter, with platelets of agglomerated particles achieving sizes above the 50 nm scale.
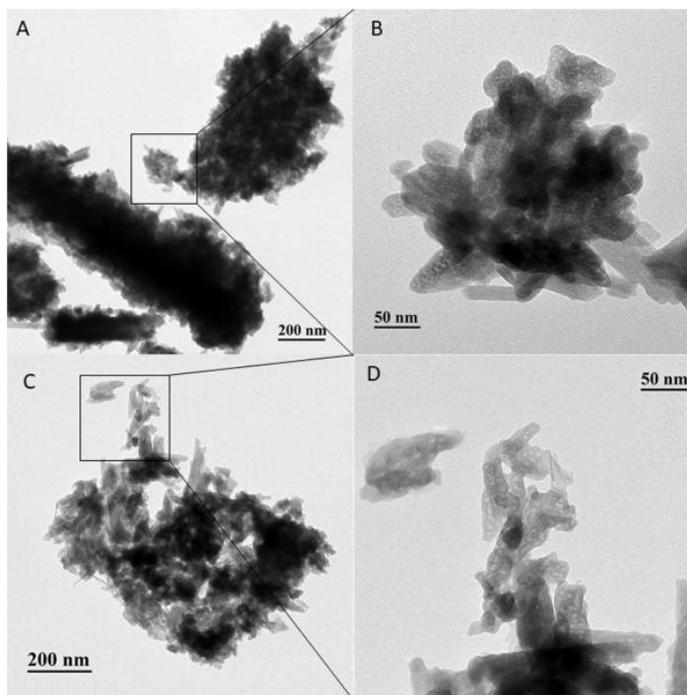
Figure 2. 9. TEM micrograph of 4-hours in situ HA. (A and B No BM, C and D mixed BM)

X-ray diffraction data were obtained for all samples in order to assess the relative crystallinity of samples as well as determine the crystalline domain sizes. Unlike the dry particle sizing method, which cannot quantify nanoscale particles near or below the optical diffraction limit or distinguish between nanoparticles and aggregates of nanoparticles. Or SEM, which cannot differentiate between amorphous and crystalline materials, XRD can determine the size of the crystalline domains of the particles, unobscured by aggregation. Representative XRD data across all synthesized HA sample types is shown in Figure 2.10, compared to the commercially available control (Figure 2.10A), measured on our instrument. Typical HA peaks are indicated by H and a carbonated HA peak is indicated by C, resulting peaks for synthesized HA displayed some shifts in peak location, this may have raised from error with detection device or from residual strain in the crystal. Here the primary characteristic HA peaks lie between 25 and 35° and are visible in all samples. Compared to the control, each of the as-synthesized HA samples (B-E)
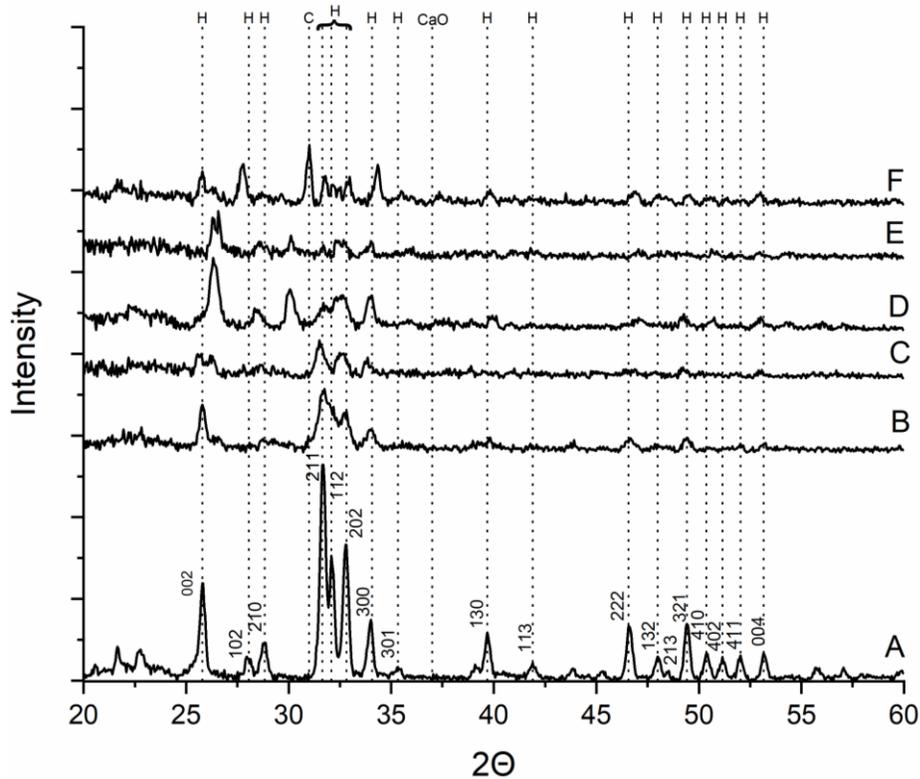
Figure 2. 10. Comparison of XRD for HA samples. A) Sigma, B) 4-hour ex situ no BM, C) 24hr ex situ milling, D) in situ no BM, E) in situ mixed media, F) in situ mixed media followed by sintering. (H Hydroxyapatite, C Carbonated Hydroxyapatite, CO Calcium Oxide)

exhibits relatively poor crystallinity as evidenced by the low overall XRD signal. The sample prepared with

in situ milling (mixed media), Figure 2.10E, appears to have the lowest crystallinity, which can be explained

in part by weaker peak within the sample. The crystallinity of this material can be improved by sintering,

during which some of the amorphous surface atoms become part of the ordered lattice. This is illustrated

in Figure 2.10F which shows an increase in the crystallinity of the aforementioned sample, following

sintering (3 hours, 950°C) [73], at Bragg angle 37° there is a small peak corresponding to CaO that has

been shown to be caused by the release of carbonated HA during sintering temperatures at 950°C and

higher [74].   The predominant size of the particles (or crystalline domain sizes) in each of the HA samples

was estimated directly from the XRD data as diffraction analysis is not as susceptible, as the other methods

employed here, to the effects of aggregation on the determination. Here the Scherrer (S) equation (1) is

employed,

$$l = \frac{K*\lambda}{\beta*\cos(\Theta)} \qquad (1)$$

29

where K (shape factor) is assumed to be 1, λ is 1.54Å, ß is the line broadening coefficient, the actual peak width at half the maximum intensity (FWHM) at the Bragg angle, Θ. The selected Bragg angle in each sample is selected to correspond to well resolved and isolated peak positions, optimizing the confidence of the calculations. All Bragg angles as within the primary characteristic HA region. The Scherrer size

Table 1. Comparison of size distribution, by size region, for HA with different *ex-situ* milling times

Sample / Milling conditions	Bragg angle (2Θ Degrees)	ß (FWHM)	Particle size (nm) S	Particle size (nm) WH	Strain WH
Sigma/ unmilled	26	0.3	31	NA	NA
4hr / *ex situ* unmilled	26	0.3	27	NA	NA
4hr / 24 hr *ex situ* milled	26	0.3	32	37	0.008
4hr / shaken *in situ* mixed media	26	0.4	22	36	0.007
4hr / shaken but unmilled	26	0.4	21	NA	NA
4 hr / shaken, *in situ* mixed media, sintered	26	0.3	28	19	0.001

analysis shows an average crystallite/grain size of 28 nm, across all sample types, with a standard deviation of 5 nm. The results for each sample are shown in Table 4. The largest sizes were for the Sigma, unmilled and 24 hr milled HA samples at 31, 27, and 32 nm, respectively. The smallest crystallite sizes were calculated for the shaken samples, with sizes for the *in situ* milled (mixed media) and media-free samples of 22 nm and 21 nm, respectively. For samples with milling processes a Williamson Hall (WH) plot was made using equation (2) to estimate size and crystal strain[75]. All variables are the same as Eq. (1) with the addition of ε strain.

$$\beta * \cos(\theta) = \frac{(k\lambda)}{l} + 2 * \varepsilon * \sin(\theta) \qquad\qquad (2)$$

With WH, a plot can be created where the Y-intercept is correlated to particle size (l) while the slope is correlated to strain (ε). Due to the poor crystallinity of the as prepared crystals, the diffraction peaks were broad and weak, making precise determination of the FWHM difficult and resulted significant uncertainty in both the particle size and strain determination by the WH equation. The calculated size and strain of the milled specimens are displayed in Table 2.4. The presence of lattice strain, as a result of milling, is seen by the shifting of maximum diffraction peak angle of 2Θ from an indexed position of 25.79 to 26.23. This has been previously observed by Aminatun et al. [75], where dry ball milling was implemented in the synthesis of HA. The results from these data may suggest that HA crystals formed during synthesis are relatively fragile. It may also indicate that simple agitation through shaking is an effective intermediate step for size reduction

2.5. Conclusion

The relatively simple and low-cost single pot method described in this chapter was used to produce synthetic but biologically relevant hydroxyapatite (HA) with scalable single batch sizes on the order of 200 grams, with typical yields of ~70%. FT-IR spectroscopy of the as-synthesized dried powders confirmed that the as-produced HA exhibited chemical similarity to naturally occurring HA. Traditional post-synthesis (dry) milling methods were compared to an *in situ* (wet) milling approach which was combined with continuous slow agitation by shaking. Dry particle sizing, SEM, and XRD data all suggest that *in-situ* milling does effectively mechanically break down the HA, reducing the particle and individual crystallite sizes to ~ 22 nm, but at the same time promotes caking of these particles, forming larger aggregates. These HA aggregates may or may not be a concern based on the desired application of the

material. Generally, the samples prepared with *in situ* milling appear very similar by SEM, and of at least equivalent quality as the *ex situ* milled sample, mimicking the overall size and chemical composition of the natural bone mineral, but were produced in roughly half the required time and at a lower overall energy cost.

Acknowledgment

CHAPTER 3

INDUCTION AND QUANTIFICATION OF FIBER ALIGNMENT IN CELLULOSE NANOFIBER THIN FILMS

3.1. Introduction

Biopolymers are known to have superior biocompatibility compared to synthetic polymers and their nontoxic nature suits tissue engineering applications[76]. Cellulose is a primary component of every plant cell wall and is the most abundant polymer on earth. Cellulose nanofibrils (CNF) is a cellulose derivative which is primarily produced using chemical and mechanical treatments on wood pulp or agricultural waste. CNF can also be produced as an extracellular biosynthetic product from Komagataeibacter *Xylinus*, a gram-negative bacterium that belongs to acetic acid bacteria (AAB) family[28]. Aquatic organisms such as algae and tunicates are examples of marine sources of CNF[77, 78]. CNF offers a diverse range of properties including crystallinity, high specific area, anisotropy, barrier properties, and chemical reactivity. From a biological standpoint, it also benefits from critical features such as biocompatibility, biodegradability, and lack of toxicity as a biopolymer [79]. CNF is known for its outstanding mechanical properties and reinforcing characteristics [80]. The anisotropic character of CNF can lead to fiber orientation, impacting CNF's modulus of elasticity and tensile strength. In nature, cellulose fibrils are present in the outer cell wall layer of plants and are naturally aligned to create a strong and durable structure[81].

CNF is widely used in biomedical applications and several reviews highlight current and potential biomedical applications of cellulose nanofibrils from various sources [82, 83]. Some of the major biomedical applications include: 1) tissue engineering [79] wound healing [84] and 3) drug delivery [85]. Creation of bone scaffolds is a particularly promising tissue engineering area due to the tunability of the

CNF mechanical properties to match mechanical properties of native human bone [86, 87]. The size-scale of CNF fibrils coupled with the ability to modify its bioactivity via surface chemistry [88] or the addition of other bioactive components such as hydroxyapatite in composite biomaterials [89] offer an exciting opportunity to mimic the extracellular matrix organization of bone tissue for the development of engineered bone scaffolds.

Within tissue engineering applications, modulating the mechanical properties of the engineered scaffold are critically important. Controlling the degree of fiber alignment in CNF-based engineered constructs positively correlates with mechanical properties [90]. Beyond mechanical properties, cellular interactions such as cell polarity and cell elongation are directly influenced by fiber alignment of the contact surface[42]. For instance, CNF based tissue scaffolds fabricated by electro-spinning have demonstrated enhanced cell alignment leading to altered cell behavior including significantly affecting cell behavior including differentiation and adhesion [91]. Bone possesses a hierarchical and anisotropic structure composed of collagen fibers and Hydroxyapatite mineral. Currently, most bone regenerative treatments focus on increasing bone mass, while taking advantage of the native oriented structure in the bone scaffold. The limited availability of suitable cadaver has inspired the exploration of engineered alternatives. Mimicking the oriented extracellular matrix (ECM) structure of natural bone remains challenging[13, 92]. Previous work has demonstrated that manipulating scaffold morphology leads to positive bone cell stimulation. Additionally, the inclusion of nanoparticulate HA has been shown to enhance bioactivity resulting in improved integration of implants with surrounding tissue [22][23].

Fiber alignment can be achieved by various techniques including drawing technique[19], electromagnetic (EM) fields [20], and spinning induced alignment [21]. Although these methods are effective, the underpinning physics limit their applications. For example, electromagnetic methods restrict the development of composites as the additional material must have similar dipole characteristics as CNF

to avoid separation. This eliminates the possibility of adding mineral oxides with homogenous distribution for increased stiffness and biocompatibility. Similarly, hydrodynamic alignment methods require precise control of fluid viscosity and nozzle velocity and are generally not well suited for high concentration suspensions. In thin-film polymer science, it is common to dry films on an impermeable substrate. Furthermore, pinning opposite ends of an immobilized film on a substrate has been shown to result in CNF fiber orientation due to internal forces exerted on the individual fiber due to contraction caused during drying, but this method is barely tunable as it only relies on internal forces[19]. Additionally, most of these methods were only applied to pure CNF and their feasibility for CNF composites are yet to be explored.

One of the most sought after composites for bone regeneration is CNF/HA composites[93]. Hydroxyapatite makes up to 70% of the bone and its bioactivity promotes osteoconductive behavior and tissue integration in implants[94, 95]. Considering the oriented matrix of collagen fibers in bone microstructure , fiber alignment is an important prerequisite to spur bone regeneration[96]. To aid in the development and characterization of these composite engineered materials, a non-destructive technique with sensitivity of fiber alignment is required. The method described here is based on the application of a controllable unilateral elongational force applied via a deformable latex substrate during the CNF drying process to create orientated CNF films. Additionally, reducing the water content of the starting CNF suspension increases the adhesion of the CNF slurry to the latex substrate enabling even greater transmission of the alignment force. The utility of this method for fiber orientation in more complex CNF-composite films was also explored with up to 10% (dry basis) mineral additives (hydroxyapatite). Here, we used Polarization Light Microscopy (PLM) and the innate birefringence of CNF to spatially map the degree of fiber orientation using the Birefringence Orientation Index (BOI) in a custom ImageJ macro. Tensile tests were performed to evaluate internal fiber alignment after stretching and Scanning electron

microscopy (SEM) images of the network were acquired to visualize surface alignment of nanocellulose fibrils.

3.2. Experimental section

All films were prepared using CNF suspensions in water (3 wt.%), obtained from the University of Maine Process Development Center. The CNF was prepared from chemically bleached northern softwood pulp by mechanical refining, and the average fiber diameter is 20–500 nm[97]. Hydroxyapatite (HA) in water (15 wt.%) and particle size of less than 50 nm was purchased from Sigma Aldrich with the surface area ≥80 m^2/g and used without modification. Latex bands, used routinely for physical therapy (Thera-Band, 4.6 lbf @ 100% elongation), were implemented without modification as the deformable substrates for this study.

3.2.1 Thin film preparation

The stock 3 wt.% CNF suspension was diluted to 1.5 wt.% solids in distilled water to decrease the viscosity and ease the spread of the CNF solution. Nine grams of the resulting CNF suspension was spread using a standard laboratory spatula on a 2 x 5-inch latex band. The latex band was taped on all edges to a hard flat rigid surface to ensure constant tension in the latex band and avoid dripping of the approximately 1 mm thick CNF films. These samples were left to dry in ambient room conditions overnight and were labeled as "unstretched".

The "stretched" pure CNF films were prepared following the same deposition process as above but were placed under a box (STP) to reduce air flow for 3 hours to decrease the sample moisture content
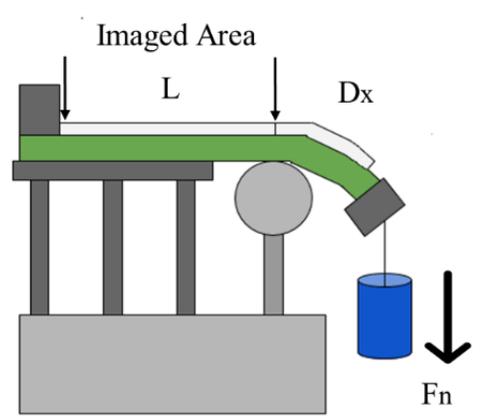
Figure 3. 1. Schematic of the unilateral stretching force apparatus for aligning CNF samples using constant uniaxial force

by approximately 30% (by weight). The reduction in moisture content increases adhesion sufficiently to allow for both the latex substrate and the CNF film to be stretched during drying. At this stage, the latex band was stretched lengthwise by applying a controlled force to one end while the other end was fixed (Figure3. 1). The samples were left to dry at STP conditions under the hood overnight. The hydroxyapatite/CNF composite films were fabricated in the same way but with the addition of HA paste to the CNF suspension with a 1:10 weight ratio, followed by magnetic stirring at 200 rpm for 4 hours, to ensure adequate dispersion of the HA into the CNF network. Dried films were carefully peeled off the latex and stored in a dry place for characterization. In order to achieve the highest level of orientation and to determine the effect of an applied force on fiber alignment, a series of samples were prepared with applied forces ranging from 0 to 11.1 KN.

3.2.2 Polarized light microscopy

Polarized light microscopy (PLM) was used to map the fiber orientation of the prepared films. A standard Olympus IX73 inverted microscope, equipped with a 10X 0.4NA air objective and Amscope color (CMOS) camera, was used for imaging of all samples. Two broadband linear polarizers were crossed above and below the sample stage thereby eliminating all light transmission. A 530 nm full-wave retardation plate was fixed in a 360° rotation mount above the stage but below the first polarizer. Using this

configuration, commonly used in mineralogy [98], the 530 nm full wave plate introduces an optical path length difference of 530 nm for light of this same wavelength in the incident linearly polarized white light. These green photons (530 nm) therefore remain linearly polarized and are fully attenuated by the subsequent crossed polarizer, whereas all other wavelengths are elliptically polarized. As a result, all other wavelengths pass through the crossed polarizer combining to create magenta-red color using Newtonian color addition/subtraction. When a sample is introduced, the birefringence introduces a phase shift proportional to the interaction of the light relative to the optical axis of the birefringent material. This interaction results in either positive or negative interference when combined in the analyzer of the PLM microscope resulting in blue (additive) or yellow (subtractive) colors. To acquire images, one of the eye pieces was replaced with the Amscope camera and the multichannel (RGB) color information of the CMOS channel was recorded. Three samples of each type were tested, where 8 areas of each sample were imaged.

To obtain quantifiable isotropic information from the CNF films, control of the relative angles of orientation between the waveplate and the CNF sample orientation is required. Rectangular CNF films were fixed onto the microscope stage with the long axis (applied force axis, see Figure 2) parallel to the horizontal edge of the stage. RGB images are acquired at both +/- 45° rotation of the 530 nm full wave retardation plate with respect to the stage-mounted sample to be used in the BOI analysis.

3.2.3 BOI analysis

Birefringence imaging is routinely used to map inhomogeneities in lithographic samples [26]. More recently, this common technique has been adapted, where specific digital color channels are used to enhance and quantify birefringence contrast, referred to as the Birefringence Orientation Index (BOI)[27]. Specifically, the BOI index relates the relative intensity of the red and blue color channels to the positive or negative birefringence of the sample.

The BOI analysis was performed with a custom image processing algorithm using ImageJ software[28]. A schematic depiction of the step-by-step image analysis process is shown in Figure 3.2. Here, The RBG images, at both +45/-45°, were separated into their respective RGB color channels. The green channel images were used as a mask to reduce noise from the set-up due to the use of a 530 nm full wave retarder plate which extinguishes green wavelengths in the crossed polarizers in the absence of a sample. As a sample, CNF is a birefringent material, therefore when probed with linear polarization, the birefringence of CNF shifts the interfering wavefronts in the crossed analyzer resulting in either blue or yellow interference colors [29]. All BOI calculations used the blue channel images. The blue channel
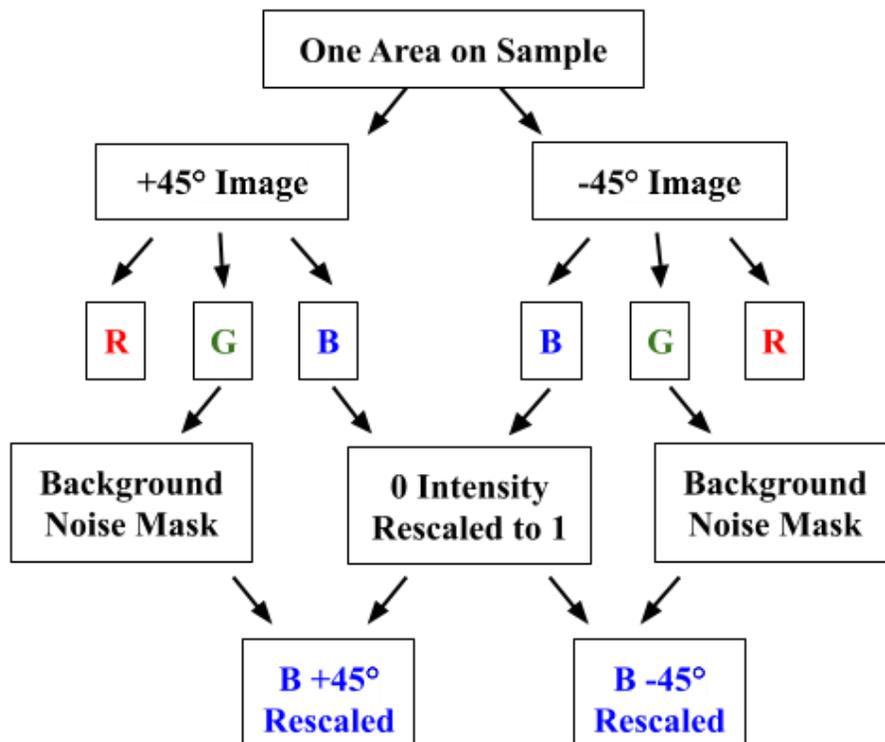
Figure 3. 1.BOI calculation process flow chart.

images were filtered using the green channel as a mask to remove noisy pixels and the 8-bit images. The masked images were rescaled 1-256 to eliminate 0 as a pixel value.

The BOI map was generated by using equation 1 where b is the pixel intensity of the blue channel at -/+45°. Resulting BOI maps were smoothed using a median filter with a radius of 1. The histograms of

each BOI image were recorded and normalized for direct comparison of BOI values. A BOI value close to zero indicates no minimum to no alignment whereas values of - 1 and 1 represent maximum orientation.

$$BOI = \frac{b_{-45} - b_{+45}}{b_{-45} + b_{+45}} \qquad (1)$$

3.2.4 Fiber Orientation Analysis

Surface morphology and fiber directionality were investigated by Scanning Electron microscopy (SEM), using a Zeiss NVision 40 Microscope. Three SEM micrographs of each sample were obtained at 3 KV with 500 X, 1KX and 5KX magnification. The characterization of the nanofibril orientation was performed using OrientationJ, a plug-in for ImageJ developed at the École Polytechnique Fédérale de Lausanne (EPFL)[99]. Gray scale SEM images were loaded in ImageJ. A Fourier transform function with Gaussian window of 1 pixel was used to make sure all fibers are taken into account. [30] The distribution of the nanofibril orientation generated by OrientationJ was centered around zero. In this analysis a Gaussian window size(σ) of 1 was used to perform the directionality analysis.

3.2.5 Mechanical Properties evaluation

Tensile tests were performed using an Instron universal testing machine (Model 5942, INSTRON Instruments, Norwood, MA, USA) with a 500 N load cell. 3 replicates of each sample type were cut into a dog-bone shape with the gauge length of 20 mm (20 mm width and 10 mm width of the neck-down). The crosshead motion speed was adjusted to 2 mm/min. Both tensile modulus and tensile strength of the samples were calculated from the load–deflection curves.

3.3 Results and discussion

3.3.1.BOI calculation

In this method, the alignment of fibers is directly affected by the longitudinal force applied to the deformable substrate. The force is applied to the sample once the solution is well adhered to the latex substrate (after losing 30% of its initial water content). The amount of force applied to stretch the wet sample was quantified by measuring the maximum longitudinal force required to fully stretch the band without breaking the sample. For each weight applied, the amount of BOI was calculated accordingly. Figure presents the BOI value of films corelated to the amount of force applied to latex band by a linear equation The results of the force optimization experiments indicate that the average BOI increased from 0.1 to 0.82 at maximum force applied. When the longitudinal force exceeded 10.2 N, the sample failed to form a continuous film, fractured and delaminated from the latex support material.

Table 3. 1Average BOI values (+/-standard deviation) achieved by applying different forces and corresponding elongation ratios.

Force(N)	Average BOI	Stretch Ratio
0	-0.1±0.14	0
4.4	-0.24±0.06	0.64
8.8	-0.57±0.07	1.29
10.2	-0.80±0.05	1.5
11.1	NA	NA

Figure 3.4 demonstrates representative PLM images of unstretched and stretched samples by applying maximum force. Unstretched samples had visual shifts in color due to CNF birefringence. The apparent color shift of the stretched CNF samples was generally dominated by a single color and appeared more uniform across the sample area indicating that the fibrillar structure of the CNF is more uniformly arranged.
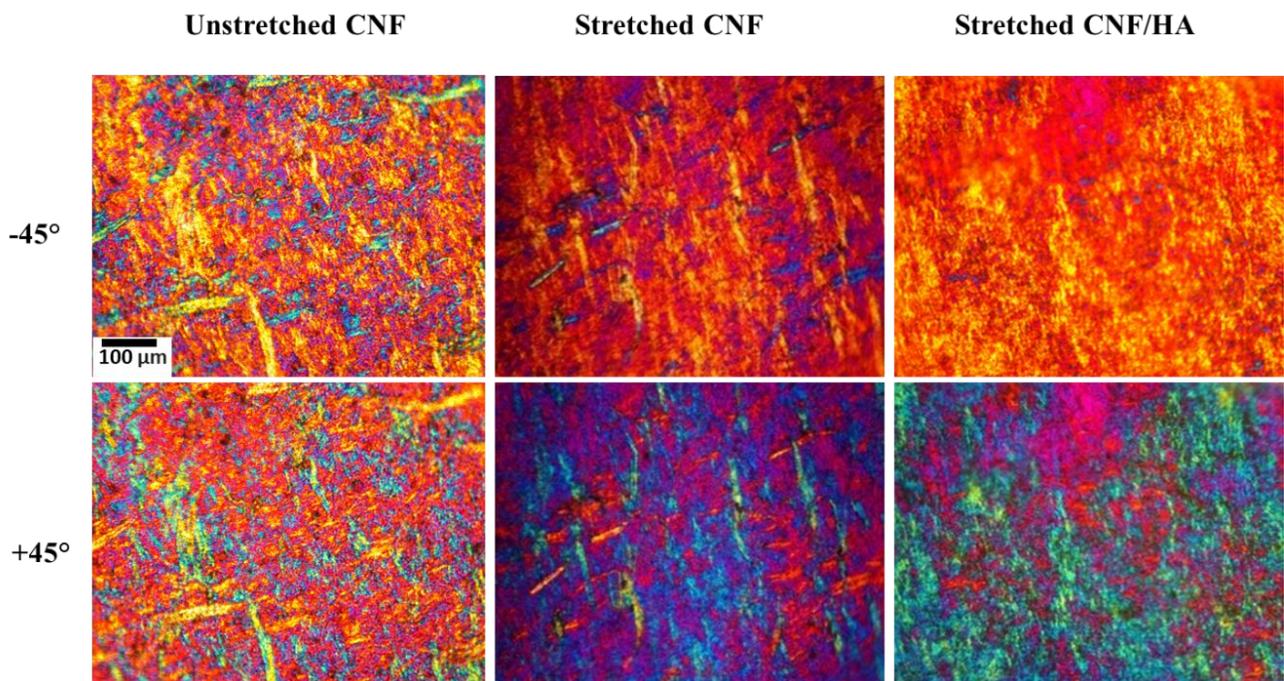
Figure 3. 2.Raw representative PLM image set. Images acquired at -45°(top) and +45°(bottom) for unstretched and stretched samples
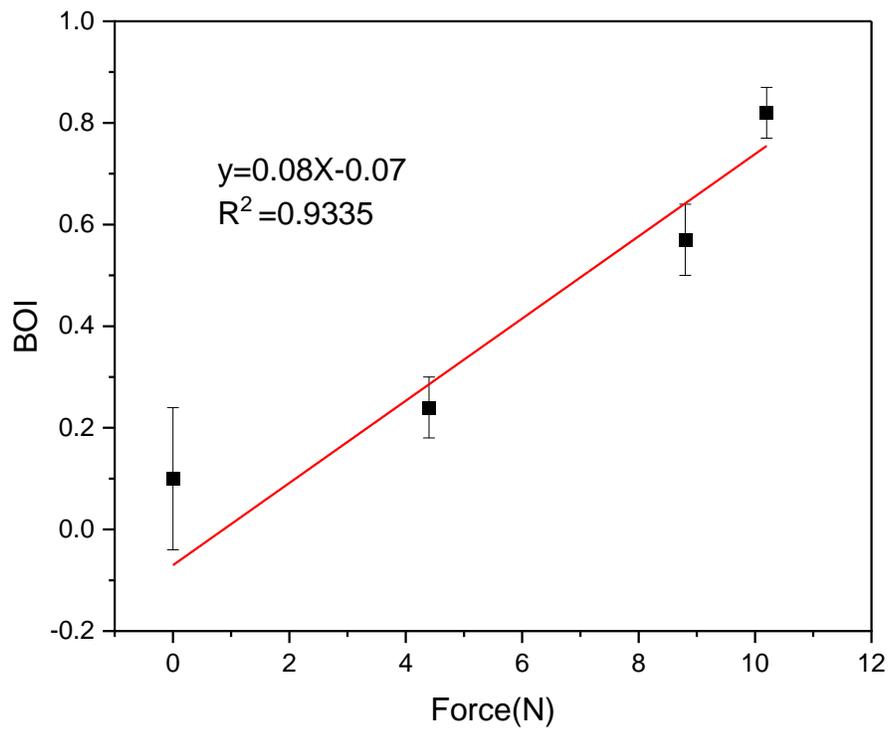
Figure 3. 3. A linear regression of BOI as a function of applied force

BOI maps, generated by method are shown in Figure 3.5.a. Here negative and positive birefringence are represented by black (-1) and white (+1), respectively. Both extremes indicate high fiber orientation whereas values closer to 0 indicate non-oriented samples. Highly oriented samples are expected to appear as dominantly black or white depending on the degree of positive or negative birefringence. Figure 5.a shows that stretched samples have a black dominant BOI close to -1. Representative normalized BOI histograms are shown in Figure 4b and 4c. Comparison of the BOI histograms clearly illustrates that stretched CNF films have a BOI skewed towards -1; whereas the unstretched CNF samples lack any dominant BOI feature.
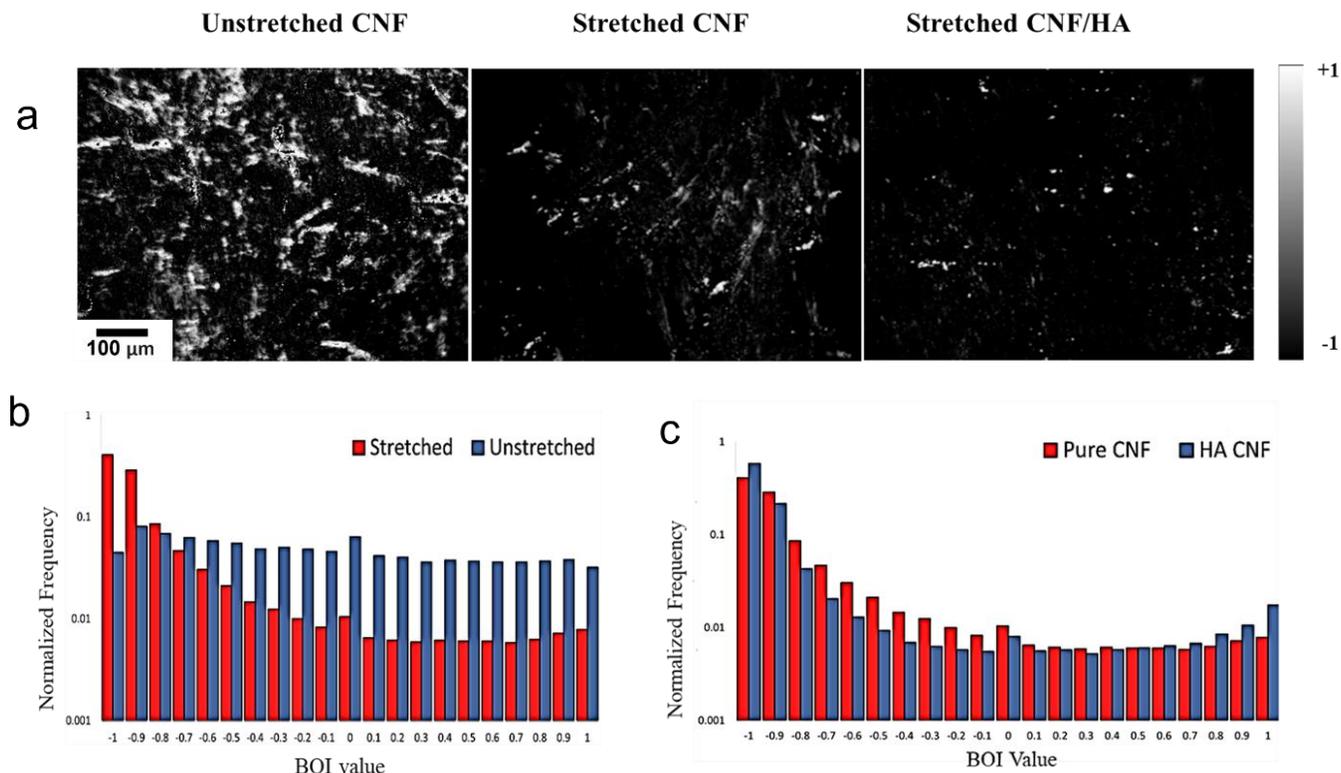
Figure 3. 4. a) Representative BOI maps of stretched and unstretched samples. b) Comparison of normalized BOI frequency distribution of stretched and unstretched CNF films. c) Normalized BOI frequency distribution of stretched composite CNF/HA vs. stretched pure CNF

The average BOI value for stretched films was -0.80; whereas the average BOI of unstretched samples had a value of -0.11, suggesting a significant increase in birefringence, indicating greater fiber orientation. In order to demonstrate the robustness of this sample preparation method, HA was included in the initial slurry (10% by dry weight). The resulting PLM data suggest that the presence of HA did not significantly alter the BOI values relative to pure stretched CNF as demonstrated by both the BOI image Figure 3.5 and histogram Figure 3.5C The average BOI achieved for the stretched CNF/HA sample was -0.82, comparable to the value of -0.80 obtained for the pure CNF sample.

To further support that the BOI method is sensitive to CNF fiber orientation SEM images at different magnifications were recorded. Figure 3.6 illustrates raw SEM images at 5KX and 10KX

magnifications. Three SEM images of each film type (unstretched CNF, stretched CNF unstretched CNF/HA, and stretched CNF/HA acquired at 1KX magnification, were analyzed using the OrientationJ plugin in ImageJ to quantify the orientation of individual fibers. Polar plots of OrientationJ calculated fiber angles are seen in Figure 3.7 C where the dominant fiber angle was normalized and centered at 0° for unstretched, stretched, and HA-doped stretched CNF films. These data clearly indicate that fiber alignment in both the CNF and CNF/HA composite films exhibit increased alignment compared to the unstretched film. Resulting representative hue-saturation-brightness (HSB) color maps of Unoriented and oriented samples are shown in Figure 3.7 a and b in which oriented fibers are apparent. To better quantify the individual image data, feature orientation polar diagrams were used. Figure 3.7 C is a polar plot of fiber angle normalized and centered at 0° of the unstretched CNF, stretched CNF, and HA-doped stretched CNF films. These data indicate that fiber alignment in both the stretched CNF and stretched CNF/HA composite films exhibit increased alignment compared to the unstretched film.
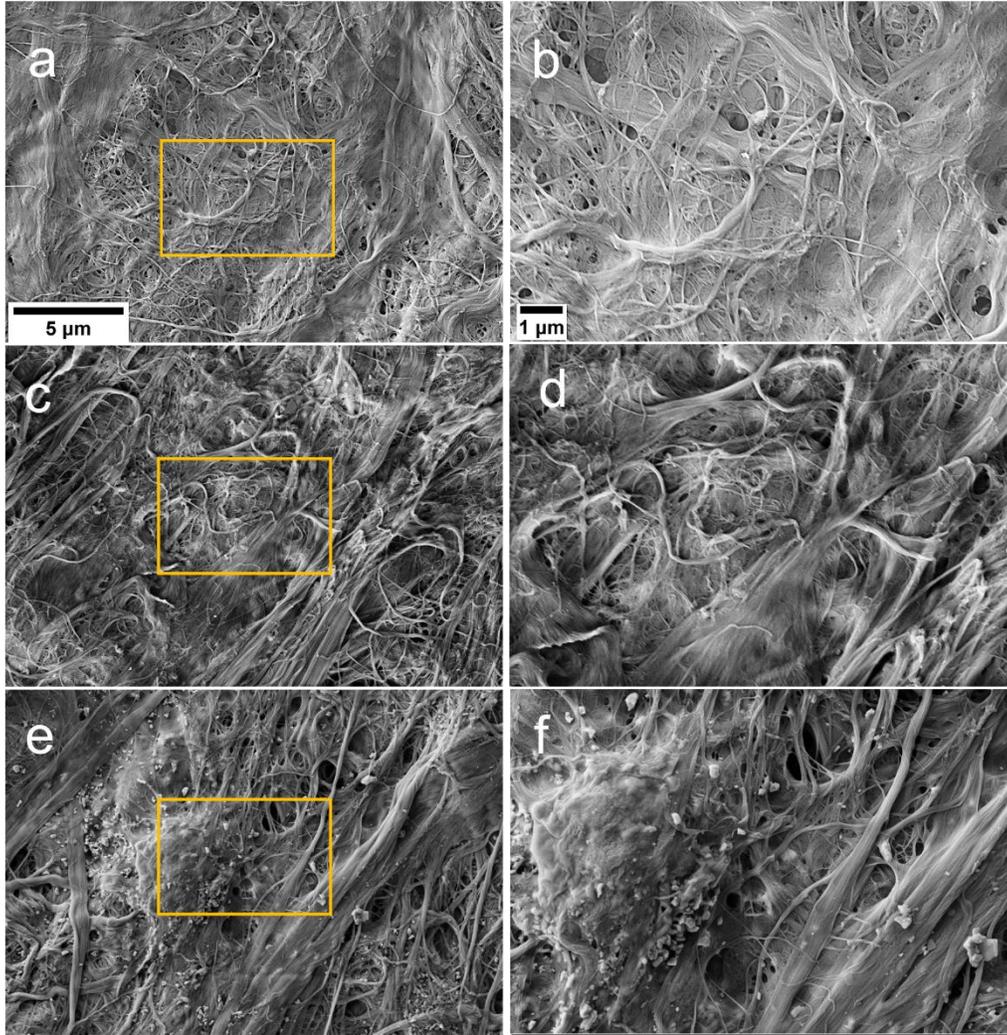
Fig 3.6. Representative SEM images acquired at 5KX (left) and 10KX (right) magnification of a-b) Unstretched CNF film, c-d) Stretched pure CNF film and e-f) Stretched CNF/HA film
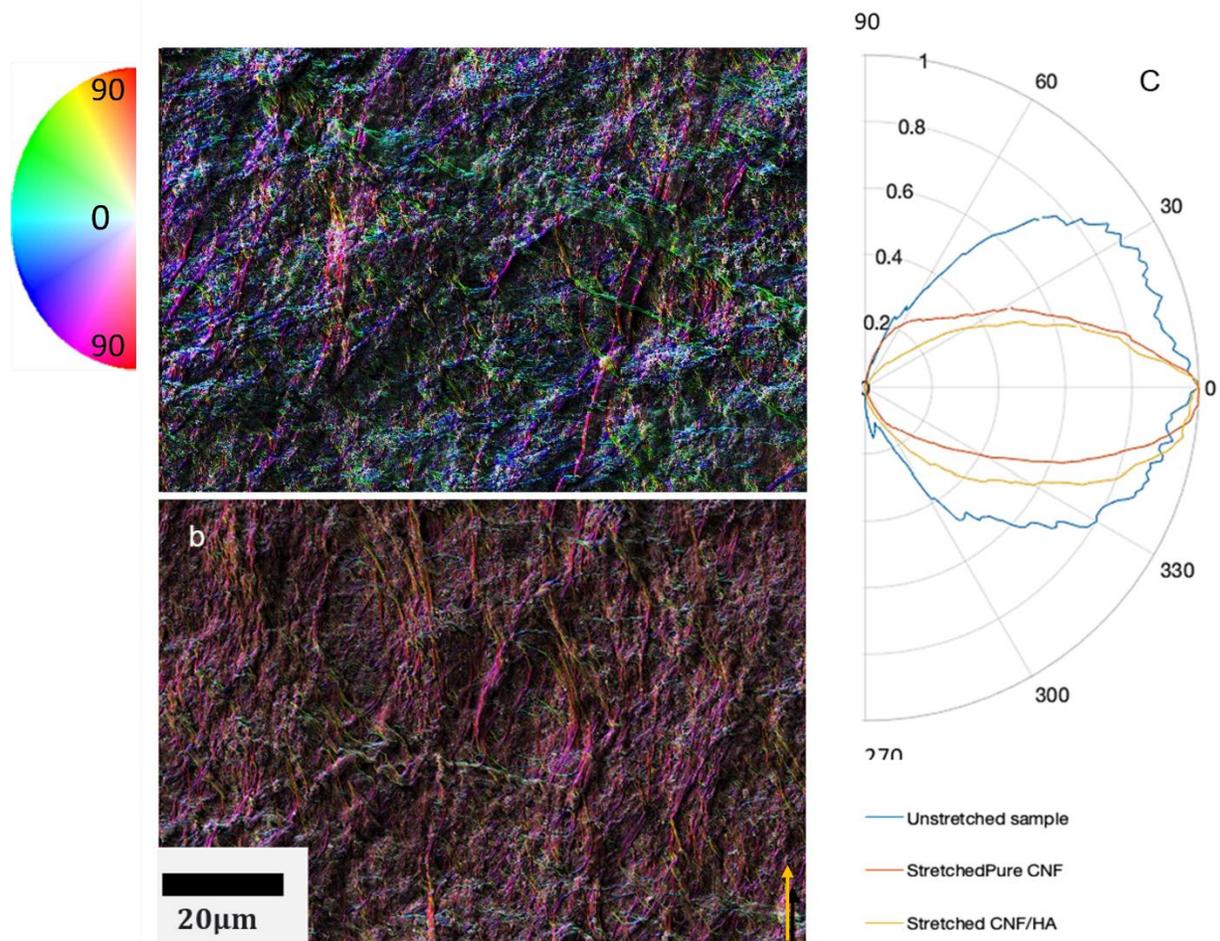
Figure 3. 7.OrientationJ analysis results: Representative color-coded images of the surface of
a) unstretched CNF film, b) stretched CNF/HA film and c) Polar plot of fibril distribution of
angles normalized around 0° for stretched and unstretched CNF samples (n = 3).

Figure 3.8 represents modulus of elasticity and tensile strength values for the pure CNF and

HA/CNF films. The results of the tensile test showed that the tensile modulus of both stretched pure CNF

and stretched HA/CNF films significantly increased (p value < 0.05), which based on prior literature

indicates internal alignment of fibers [100]. Tensile strength values showed that the addition of HA in both

stretched and unstretched samples significantly reduces the tensile strength likely due to the HA

nanoparticulate disrupting the hydrogen bonding between nanocellulose fibrils. Although the tensile strength decreased for the composite CNF/HA material, the tensile strength remains similar to the unstretched CNF. The elastic modulus is significantly increased for stretched CNF films and there was no significant difference between the modulus of elasticity of stretched CNF and stretched CNF/HA. This is in agreement with the previous data that both pure CNF and CNF/HA films had the same BOI value suggesting that they have same level of orientation. Collectively, the tensile strength and elastic modulus suggest application of longitudinal force results in internal alignment of CNF fibrils.
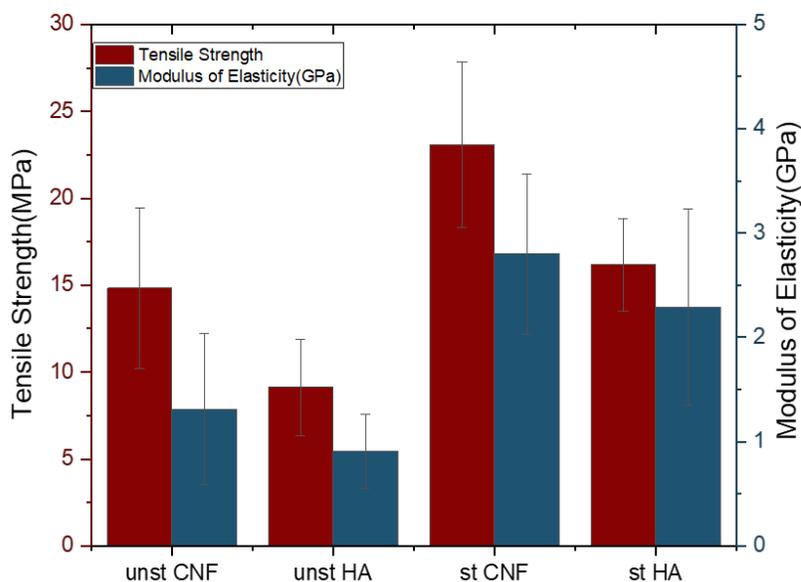
Figure 3. 8.Tensile strength and modulus of elasticity of films

3.4 Conclusion

In this chapter, we developed and tested a novel, cost effective and tunable method to induce fiber orientation in CNF and CNF/HA films. A BOI index method was adapted to compare PLM data which showed that our method significantly increased fiber orientation in both pure CNF and hydroxyapatite incorporated CNF films. Mechanical testing showed that tensile strength and tensile modulus significantly improved by stretching implying internal alignment of fibers in stretched samples. SEM images were used

to validate the BOI results and provide insight into the narrow orientation distribution for stretched samples compared to unstretched samples. Both PLM and SEM results showed that incorporating HA into the CNF matrix did not interfere with the fiber orientation or film consistency and they both showed fiber orientation. HA has been shown to improve bioactivity and biocompatibility of the films and its incorporation in a highly aligned oriented matrix achieved in this study can be particularly beneficial in bone regeneration studies.

CHAPTER 4

CHARACTERIZING CELLULAR BEHAVIOR ON ANISOTROPIC CNF FILMS

4.1. Introduction

In tissue regeneration, the development of organ-specific architectures to replicate the original function is critical[101-103]. The extracellular matrix (ECM) regulates the cellular physiology, its structure facilitates cell adhesion and stimulates biophysical signaling cascades. Some types of human tissue such as connective tissue and vasculature require significant order and alignment in the ECM structure in order to function properly[104]. When this highly oriented ECM structure is disrupted, the cells will not be able to assemble their cytoskeleton to elicit the appropriate biochemical signals[105] .

Bone tissue has a hierarchical and anisotropic structure composed of hydroxyapatite and collagen fibers contributing to the unique mechanical properties of bone. Some pathological conditions such as osteoporosis and osteopetrosis [104] cause a disruption to this anisotropic ECM that eventually increases the risk of bone failure. During the regeneration process, bone needs to maintain its oriented microstructure in order to prevent fracture. Currently, most of the bone regenerative treatments exclusively focus on increasing bone mass, ignoring the necessity of oriented structure in bone tissue. Hence, restoring the bone tissue anisotropy remains a challenge yet to be overcome[106].The engineered scaffolds intended to be used in bone regeneration applications require to be architected in a way that replicates anisotropic ECM structure of bone microenvironment. Proper topography of scaffold will stimulate bone cells to proliferate as they do in native tissue.

As a sustainable source of material, CNF is a potential collagen replacement considering its inherent biocompatibility and fibrillar structure. Unique mechanical properties of CNF that makes it a potential candidate for connective tissue repair. The intermolecular hydrogen bonding between the fibers

significantly increases the mechanical properties of CNF. The mechanical properties and surface chemistry of CNF can be adjusted to suit different applications.

HA is a type of bio ceramic with a crystalline structure similar to the mineral part of the bone with outstanding bioactivity along with being resorbable and osteoconductive [107]. HA is a great candidate for bone regeneration , however its brittle nature has limited its application to non-load bearing materials[107]. Combination of HA and collagen in bone structure gives bone the perfect balance between strength and toughness. In an effort to emulate bone structure ,HA have been used as an additive to different types of organic polymers such as alginate[108], gelatin[109] , collagen[110] , chitosan[111] , and bacterial cellulose[112] . However, these efforts have been facing challenges such as biomechanical and biological properties, insufficient intrinsic incorporation, and sometimes masking of an inorganic component by an organic one[113], alongside with a poor dispersion of the HA in a polymer matrix. Thus, the need to achieve an advance composite structure that resembles bone tissue remains a challenge. In this chapter, we used the thin films attained by the procedure explained in chapter 3 to evaluate the osteoblast (MC3T3E1) cell response to the microenvironment that this material provides.

4.2. Methods

4.2.1. In vitro cytocompatibility

The cytocompatibility of the films was investigated using mouse pre osteoblast cells (MC3T3E1) cells. Preosteoblasts are precursor to osteoblast production that leads to construction of bone matrix. MC3T3E1 cells were cultured in complete media consisted of MEM Alpha 1X with 10% FBS and 1% penicillin/streptomycin. Cells were trypsinized at 80% confluency to be used for cytotoxicity assay.

Four different sample types (3 replicates of each) including pure unstretched CNF, pure stretched CNF, unstretched HA /CNF and stretched HA /CNF films were punched into circular shape to fit into a 96-

well plate. Samples were sterilized by UV light for 1 hour. Then, 100 µL of complete MEM Alpha media was added to each well and the plate was transferred to incubator for 1 hour. The media will soften the films and prevents cells from slipping off the films. After 1 hour, the media was removed and 200 µl of the cell suspension with a density of 100,000 cell per ml was added to the sterilized films. 3 empty wells were filled with 200 µl of cell suspension and labeled as control. The plates were incubated in a humidified atmosphere of 5% CO_2 at 37 °C for 24 , 48 and 72 hours. After the incubation period, cell media was removed and replaced with 100 µl fresh media and 10 µl of the 12mM MTT stock solution was added. After labeling the cells with MTT, as described above, 85 µL of medium was removed from the wells and added 50 µL of DMSO to each well and mixed thoroughly with the pipette. Then, the samples were Incubated at 37°C for 10 minutes and mixed again. A microplate reader was used to read the absorbance (OD) at 540 nm.

4.2.2. Live/Dead cell staining (FDA/PI)

In order to confirm the MTT results and compare cell viability and cell adhesion of the stretched and unstretched samples, cell viability test was performed. In this experiment, Propidium iodide (PI) and Fluorescein diacetate (FDA) were used as the live/dead fluorescent staining agents. 4 different sample types including pure unstretched CNF, pure stretched CNF, unstretched HA /CNF and stretched HA /CNF films were investigated. 3 wells with no films were used as control. Films were punched into circular shape to fit into a 12 well plate sterilized using UV light for one hour. After the sterilization, 1 mL of complete media was added to each well and then placed into the incubator for 1 hour. After one hour of incubation in media cells were trypsinized from their flasks and seeded onto the films and controls at a density of 150,000 cells/mL and culture dish was incubated for two different time periods of 24 and 72 hours.

The staining solution was prepared fresh by mixing stock solutions of 5 mg/mL FDA in acetone and 2 mg/mL PI in PBS. 8 µL of FDA and 50 µL PI solution were added to 5mL MEM Alpha 1X media without

FBS. At 24- and 72-hour time point, the culture dish was taken out of the incubator and the media was removed. Next, 1 ml the staining solution with FDA and PI was added to each and left to incubate at room temp for 5 minutes with the hood lights turned off. Next, the staining solution was removed, and each well was washed with 2 mL of PBS. After removing the PBS, 2 ml of MEM Alpha 1X media (without FBS) was added to each dish. Then, Films were imaged on the Leica wide field fluorescence microscope with a 5X objective. Each sample was imaged using a grid-based approach and 3 different areas were selected to acquire images based on how representative they were of the entire sample.

4.2.3. Nuclei and cytoskeleton staining

As it was mentioned earlier in this chapter, ECM morphology can tremendously affect cell behavior. This experiment is designed to investigate the effect of fiber orientation on cell attachment and actin/nuclei directionality of preosteoclasts. Phalloidin-iFluor 555 reagent was used to stain cellular f-actin and DAPI was used to stain nucleus.

1X Phalloidin conjugate solution was prepared fresh by adding 1 µL of the 1000X Phalloidin conjugate Stock solution to 1 mL of PBS plus 1% BSA and mixed well by pipetting. 4 different sample types including pure unstretched CNF, pure stretched CNF, unstretched HA /CNF and stretched HA /CNF films were investigated. Films were punched in circular shape to fit into a 12- well plate sterilized using UV light for one hour. After the sterilization, 1 mL of media complete media was added to each well and then placed into the incubator for 1 hour. After one hour of incubation in media preosteoclast cells were trypsinized from their flasks and seeded onto the films and controls at a density of 100,000 cells/mL and culture dish was incubated for 72 hours. Next, the cell media was removed and 3% formaldehyde in PBS solution was added to each sample and incubated under the hood at room temperature for 10-30 minutes. After the incubation period was over, 1 ml of 0.1% Triton X-100 in PBS was added to the fixed

cells for 5 minutes to increase permeability. At this stage, fixed cells were rinsed 3 times with PBS and 100 µL of 1X Phalloidin conjugate solution to each well of fixed cells. At this point, 1 ml of 5mg/ml DAPI solution was added to stain nuclei and samples were incubated at room temperature for 1 hour. Next, samples were gently washed with PBS for 3 times to remove excess phalloidin conjugate and MEM Alpha 1X media was added to each well. The samples were imaged using a Leica fluorescent microscope at Ex/Em 493/517 nm.

4.2.4. FFT Analysis of cell orientation

The FFT filter feature of ImageJ was used to quantify the degree of orientation of samples. FFT analysis allows the morphological quantification of microscopic structural alignment and pixel information of the photomicrograph is transformed into Fourier space (power spectra). Using the oval profile plugin of ImageJ, the radial sum intensities are generated for 360 radii around the center of the FFT image. To prepare images for the FFT analysis, all images went through the following process:

1- First, the split channel feature of ImageJ was used to achieve black and white images. Next, a background reduction followed by auto contrast adjustment were applied to make cell actins more visible for analysis. All images were processed with the same macro for consistent results.

2- Images were resized to 1024x1024 pixel that is recommended size for FFT analysis[114]

3- Next Using the "angle tool" of the main toolbar, the orientation angle of aligned actines was estimated. This angle will be used later to calculate root mean square (RMS).

4- By choosing the FFT option from the menu bar the black and white image was transformed into its sine and cosine components and the pixel information was mapped in terms of relative intensities along specific orientations.

5- Using the oval tool in the main toolbar a symmetrical circle was created to capture the entire FFT starburst achieved by applying FFT filter. The ring size was adjusted to ensure the ring captures

FFT starburst without including unnecessary dead space. The ring size remained the same for all images to ensure consistency across the sample analysis.

6- By using the input output plugin in ImageJ and applying its oval profile feature, a radial sum intensity graph was generated. This step will sample the specified number of angles. Here we set the number of angles to 360 to be able to detect the orientation angle with more precision. The x and y values for all 360 angles from last step was used to create a X-Y scatter plot.

7- The two peaks appeared on radial sum intensity scatter plot represent the angle of interest and the opposite angle of interest, while the troughs of the radial sum intensity represent the orthogonal angle and the opposite orthogonal angle. The angles at the peaks represent the alignment angle of the cytoskeleton. Since the cytoskeleton structures are not perfectly aligned, samples of the radial sum intensities around the four angles are taken into consideration as well as the angles themselves.

8- According to previous studies, the ratio to the mean orthogonal angle represents the amount of alignment in oriented structures[114]. The equations for the ratio to mean orthogonal angle are below.

Root mean square (RMS) = $\sqrt{\frac{\sum_{i=1}^{360} Ai^2}{360}}$ (1)

A= The radial sum intensity of each angle or Y in x-y scatter plot

$Ave_m = \frac{\sum_{j=1}^{22}\frac{Mj}{RMS}}{22}$ (2)

Ratio to mean orthogonal angle (ROA) e = $\left|\left(\sum_{k=1}^{22}\frac{\frac{Nk}{RMS}}{Ave\,m}\right) * 100\right| * -100$ (3)

M = The radial sum intensities of 22 angles, including the orthogonal angle ± 5 flanking angles and the

opposite orthogonal angle ± 5 flanking angles.

N = The radial sum intensities of 22 angles, including the angle of interest ± 5 flanking angles and the

opposite angle of interest ± 5 flanking angles. A value of 0 for the ratio to mean orthogonal angle

represents no alignment for the microscopic structures; while a value of 100 shows complete alignment

for the microscopic structures.
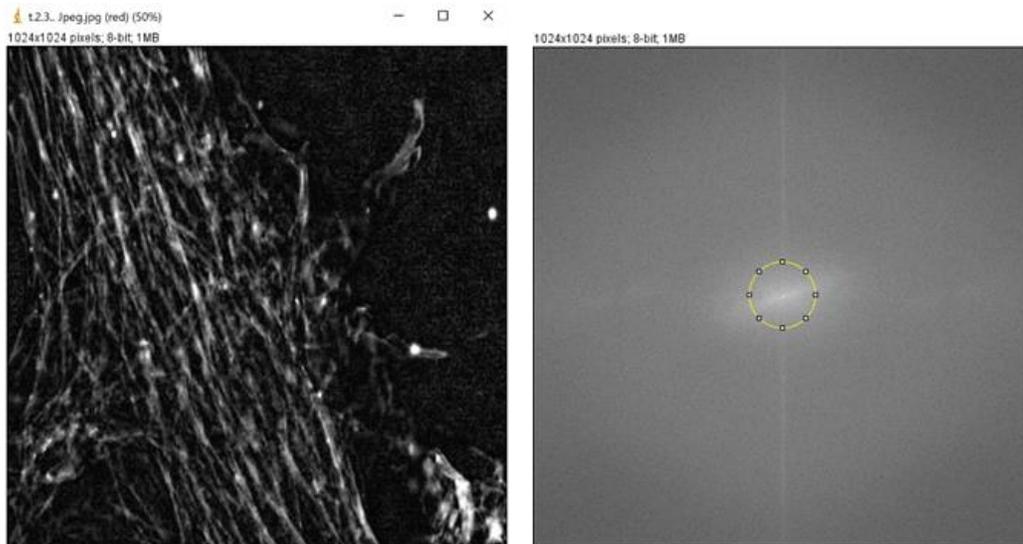
Figure 4. 2.left) Black and white image of stretched cytoskeleton acquired by flufenacet microscope.
Right) FFT filter ring analysis
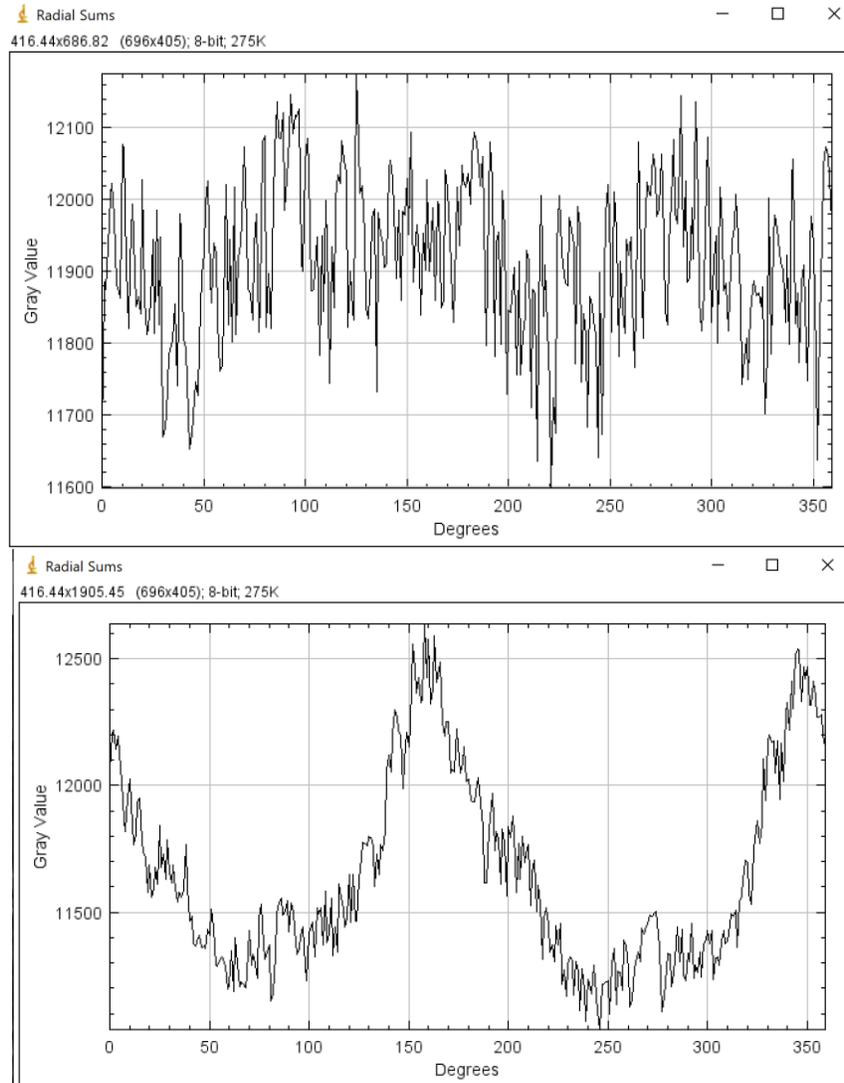
Figure 4. 3. Radial sum intensity plot of cell actins on a) unstretched films b) stretched films

4.2.5. Nuclei Circularity

Micrographs obtained from DAPI stained nuclei went through a series of image processing steps to calculate nuclei circularity. Particle analysis feature of ImageJ software was used to calculate circularity. Six images of each sample type group were analyzed, and an average circularity was calculated as shown in Figure 4.8.

4.3. Results and discussion

4.3.1. MTT Assay

Figures 4.3 and 4.4 present the MTT results reported as OD values of samples at 24- and 72-hour time points. Figure 4.3 compares the cell viability of unstretched pure CNF and unstretched HA /CNF films to the control. According to the OD values obtained at 540 nm, after 24 hours of incubation, there was no significant difference between the cell viability of unstretched pure CNF films and control (Polystyrene plate). The same result was observed for unstarched HA samples. Although the HA modified film demonstrated slight increase in OD level, however it was not statistically significant (P value >0.05) suggesting that HA did not have a major effect on cell viability after 24 hours in unstretched samples.

After 72 hours of incubation, cell viability of unstretched CNF sample significantly increased comparing to day 1 indicating cell proliferation. No significant difference between control and unstretched CNF cell viability was observed at this point. However, unstreched HA/CNF sample showed significantly higher ($P < 0.005$) cell viability compared to the control suggesting that the HA presence positively affected cell proliferation after 72 hours of incubation.

The effect of surface morphology on cell viability was also evaluated by MTT assay. Figure 4.4 demonstrates the cell viability of stretched pure CNF and stretched CNF/HA films compared to control. At 24-hour time point, OD level of stretched CNF film was at the same level of control, however, stretched CNF/HA sample showed a higher OD level comparing to control and stretched CNF sample. This observation is particularly important as it demonstrates that simultaneous effect of HA and orientation have a positive impact on cell viability even after 24 hours, while the presence of HA in unstretched samples did not have a remarkable effect on cell viability at this time.

At 72-hour time point, cell viability of stretched CNF and stretched CNF/HA samples significantly increased from day one and were remarkably higher than control, suggesting successful cell proliferation

on both films. Additionally, stretched CNF/HA showed higher cell proliferation compared to stretched CNF indicating positive effect of HA on cell growth.

Overall, MTT results revealed that stretched CNF/HA samples showed positive effect on cell viability from day 1, while positive effect of orientation in absence of HA was observed at day 3. Therefore, simultaneous presence of HA and fiber orientation can maximize cell proliferation.
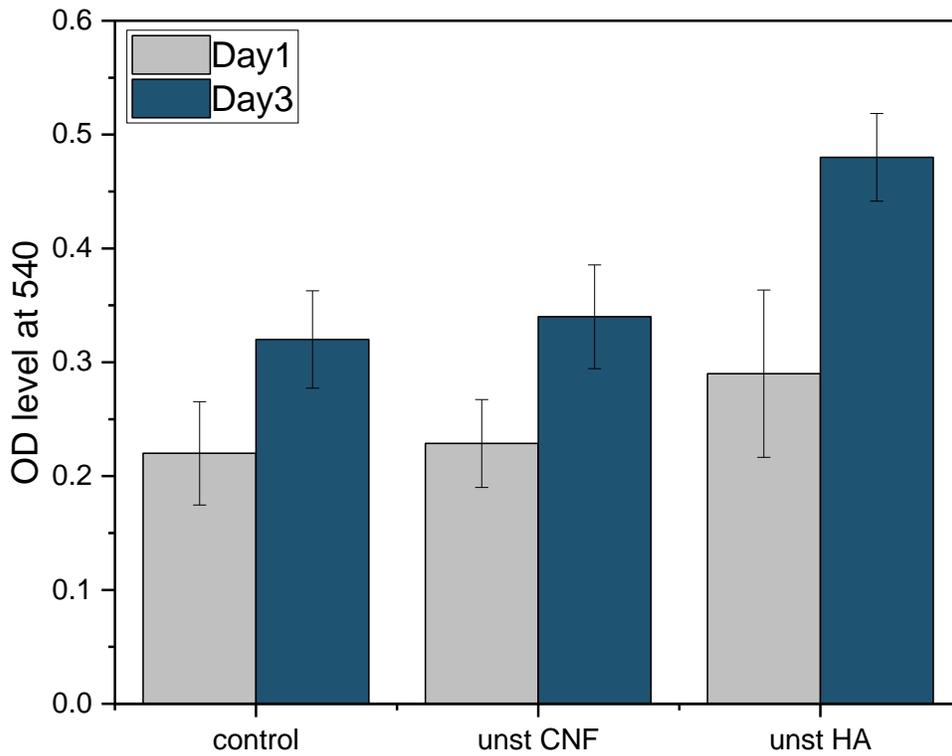
Figure 4. 4. Optical density of unstarched samples at 540 for day 1 and day 3
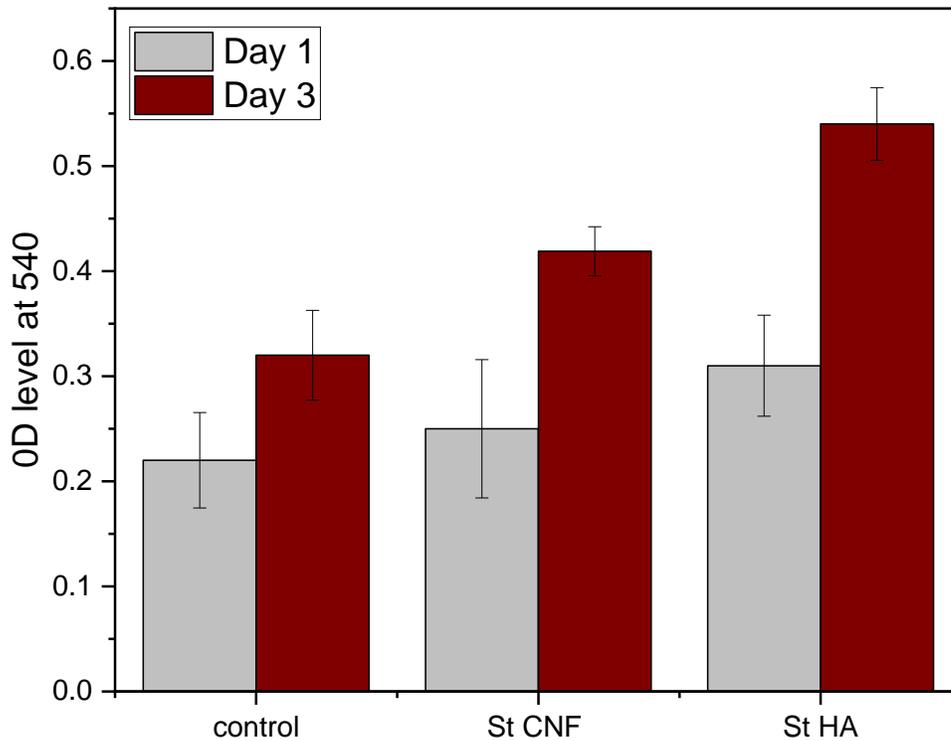
Figure 4. 5. Optical density of stretched samples at 540 for day 1 and day 3

4.3.2.FDA /PI results

Proliferation of MC3T3E1 cells was further investigated by FDA/PI assay. Figures 4.5 and 4.6 represent images of FDA labeled MC3T3E1 cells at 24- and 72-hour time points. All samples showed significant increase in number of cells after 72 hours of incubation. Autofluorescence effect of films and exposure time caused uneven illumination in acquired images. However, live cells can be easily distinguished from the background in represented figures. Study combined with MTT results suggest that the highest proliferation and cell viability is achieved by having both orientation and HA in a single film.
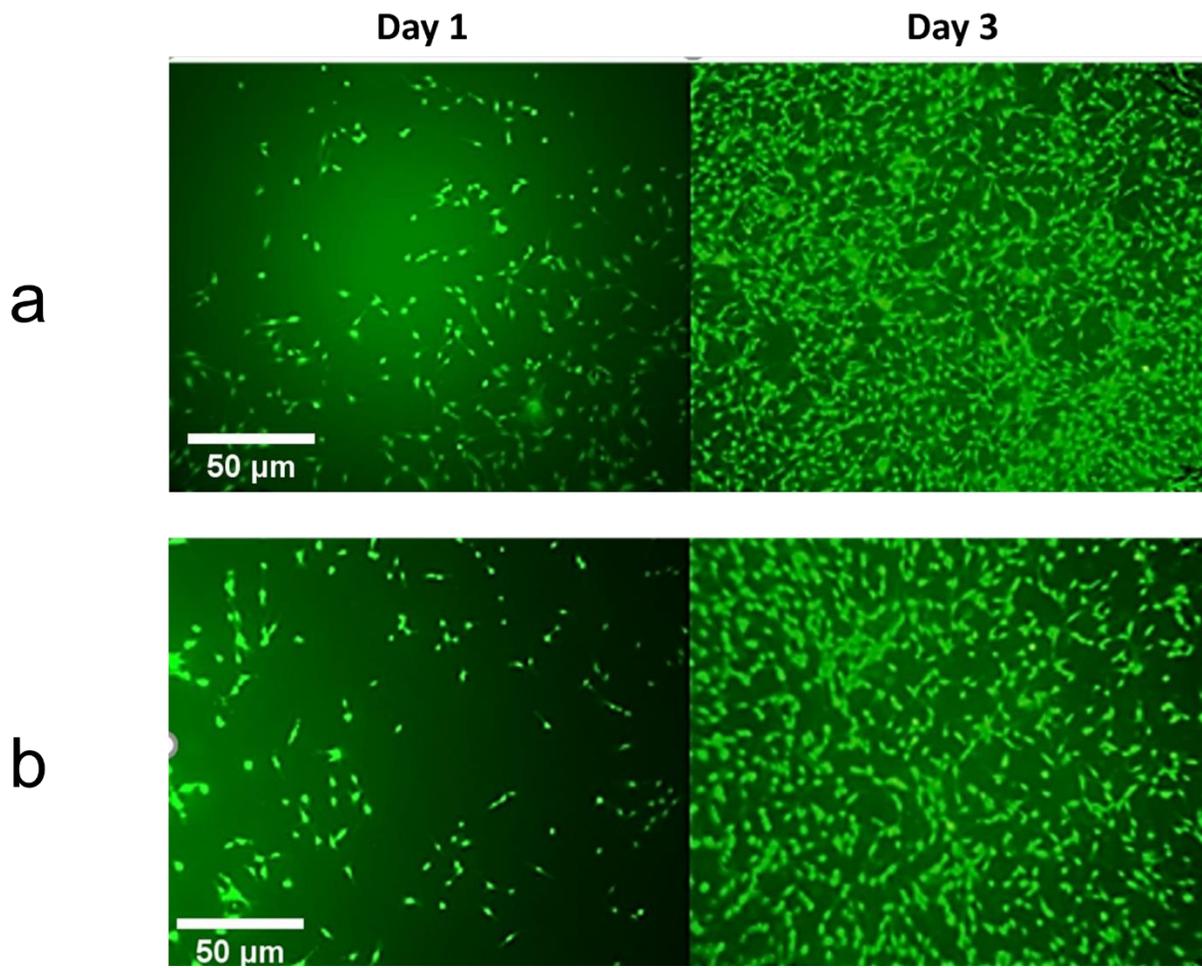
Figure 4. 5. Fluorescent images of FDA stained cells cultured on a) Stretched CNF/HA b) Stretched CNF
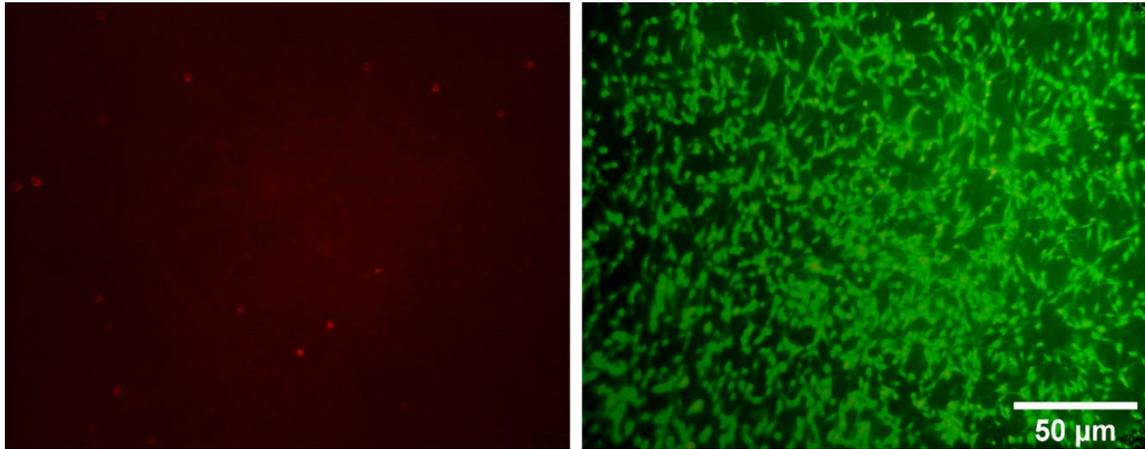
Figure 4. 6. Fluorescent images of live (green)and dead (red)cells present on the surface of stretched CNF/HA film

4.3.3. Cellular morphology analysis

Cellular orientation was quantified using FFT filter and RMO values were calculated accordingly. A RMO value close to zero indicates minimum to no orientation while a perfectly aligned structure has a RMO close to 100. Tylor et al, used this method to quantify orientation and compare directionality of different structures. For highly aligned structures such as steel wire and bamboo the RMO values were calculated at 42 and 28 respectively, whereas aligned oligodendrocytes and neurons resulted in RMO values of 8.7 and 12.6 respectively[114].

Figures 4.7 demonstrates black and white images of actin filaments and nuclei of preosteoblasts seeded on stretched CNF film acquired by florescent microscope. Actins show a dominant orientation at 45°, and nuclei are elongated towards same direction.

Figure 4.8 compares cytoskeleton and nuclei morphology of preosteoblasts seeded on stretched and unstretched films after 7 days of incubation. The Phalloidin staining in red color represent actin

filaments and blue displays DAPI stained nuclei. Cells seeded on stretched films showed a preferred cytoskeleton orientation while no dominant orientation were observed for unstretched samples. Additionally, in case of stretched films, nuclei are elongated towards the cytoskeleton direction while showing more circular and random shapes on unstretched films. The same effect was observed in stretched HA films modified and both oriented cytoskeleton and elongated nuclei were detected.
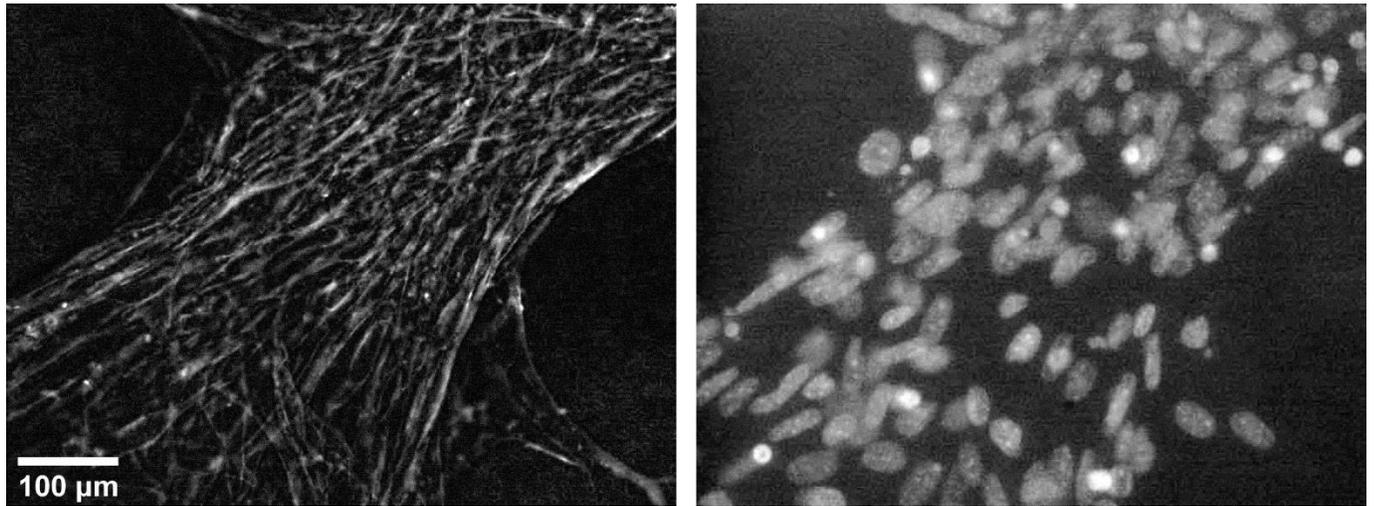
Figure 4. 7. Black and white microscopy images of cytoskeleton(left)and nuclei (right) of MC3T3E1 cells on stretched CNF films

	stretched CNF	stretched CNF/HA	unstretched CNF
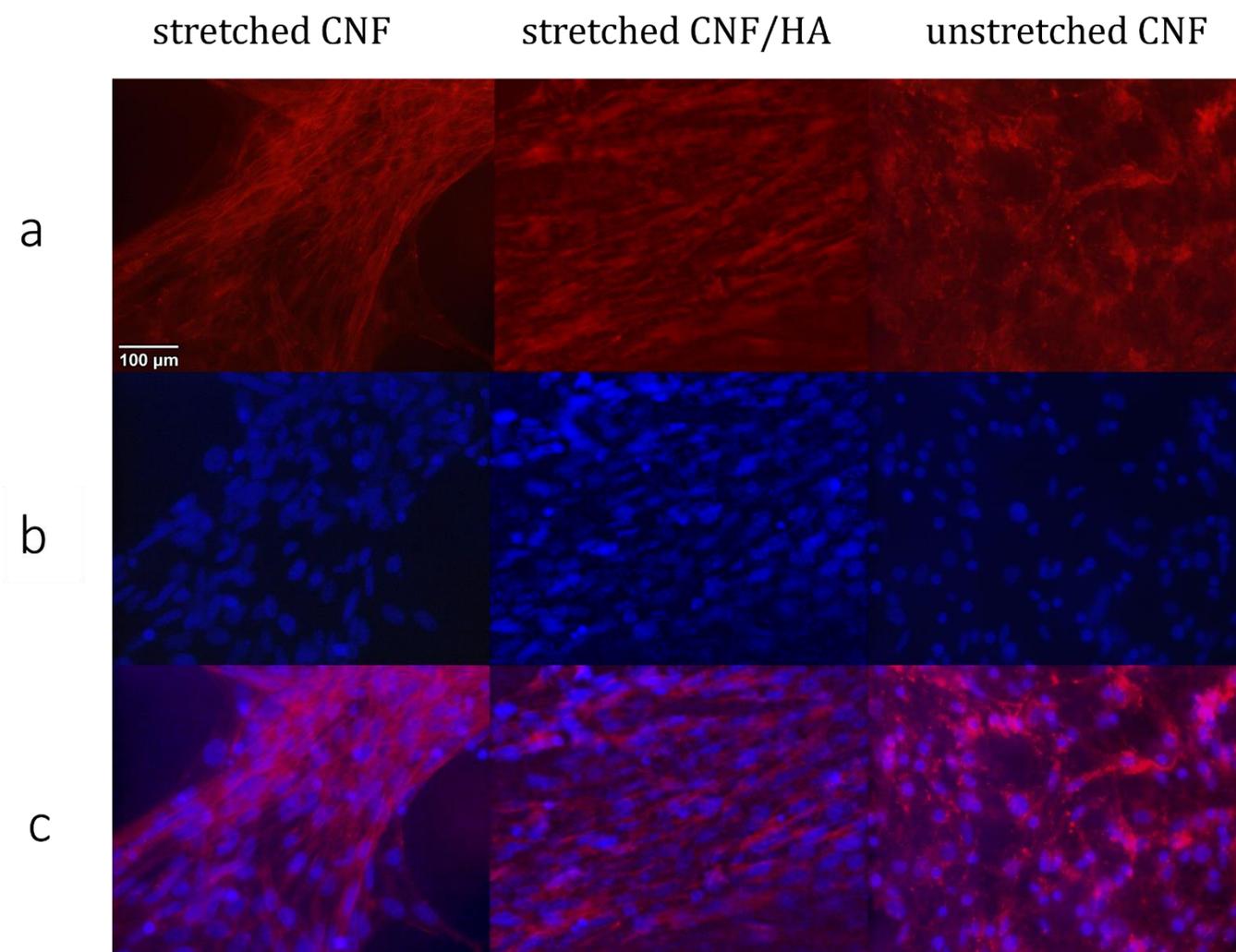
Figure 4. 8. Fluorescent microscopy images of Phalloidin (a) and DAPI (b) stained MC3T3E1 cells on films with oriented and random structures

Figure 4.9 presents quantified cytoskeleton orientation reported as RMO values. The average RMO value for unstretched Pure CNF and unstretched CNF/HA samples were calculated at 1.05 and 1.15 respectively that is significantly lower than the RMO values of stretches samples(P<0.05). The average RMO value of stretched CNF and stretched CNF/HA were 10.7 and 10.13 respectively. The difference between RMO value of cells cultured on stretched CNF and stretched HA/CNF was insignificant(P>0.05) suggesting that that both microenvironments had the same effect on cell alignment.
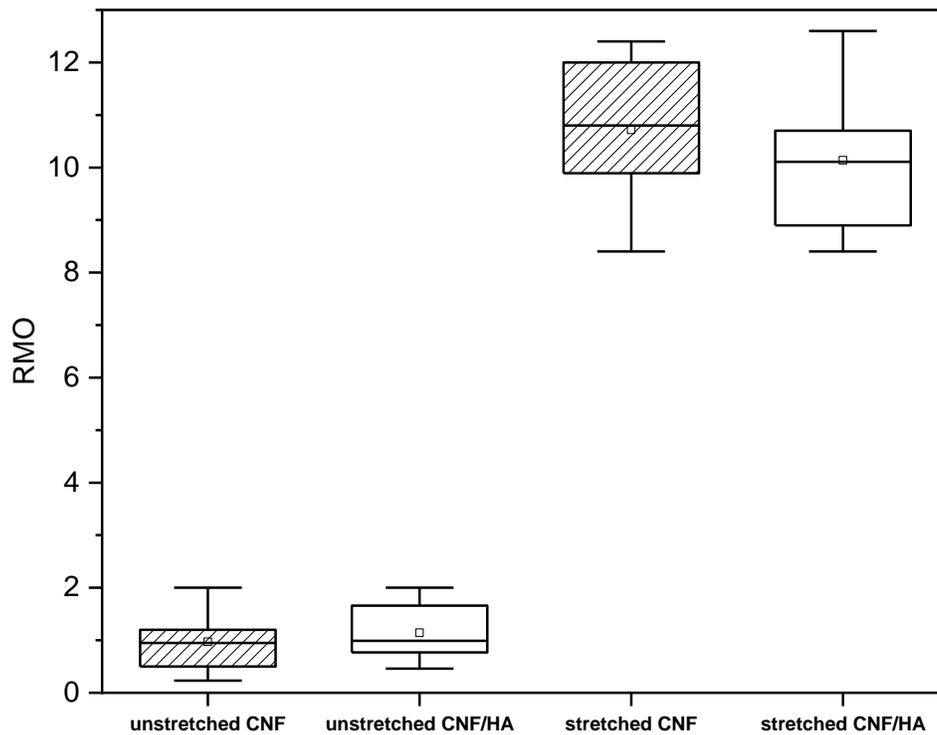
Figure 4. 9. Average RMO values of cells cytoskeleton seed on films

This finding is in agreement with previous data in chapter 3 that showed stretched HA/CNF samples had the same BOI compared to stretched CNF. This analysis revealed that cell morphology is significantly

impacted by fiber orientation and the films with aligned fibers induced alignment to the cytoskeleton and cause elongated nuclei shape.

4.3.4. Nuclei circularity

Nuclei circularity analysis of cells seeded on 4 types of films are illustrated in figure 4.10. Circularity is defined as a value between 0 to 1. A perfectly round object has a circularity close to 1 and value of 0 is attributed to a straight line. Xuyan et al. demonstrated that the nuclei aspect ratios are directly affected by surface orientation and fiber directionality at nanoscale can affect nuclei elongation[115]. They showed that cells cultured on oriented matrix had higher aspect ratio(or lower circularity) compared to random fibers[115].
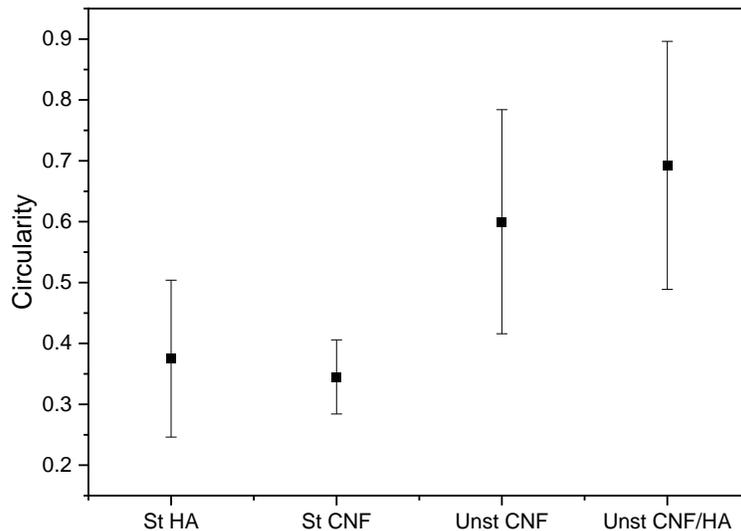
Figure 4. 10. Circularity analysis of nuclei

Circularity values represented in figure 4.10 denote that preosteoblasts cultured on oriented CNF films had significantly lower circularity (P<0.05) comparing to unstretched CNF films. The same result was

observed for HA incorporated samples. Circularity value of both stretched CNF and stretched CNF/HA were almost half of the unstretched samples of each type indicating the elongated morphology of nuclei on stretched films. We did not observe a statistically significant difference between the nuclei circularity of HA modified samples compared to pure CNF films suggesting that the ECM alignment was the dominant factor in nuclei elongation rather than mineral composition.

4.4. Conclusion

In this chapter we performed biological assays to evaluate the effect of fiber orientation and mineral composition of CNF thin films on cellular proliferation and morphology. MTT and FDA/PI assays demonstrated that oriented CNF/HA films provided a favorable microenvironment for the cells to proliferate with no cytotoxicity being observed. Cytoskeleton and nuclei staining confirmed that cells cultured on oriented samples are being redirected to a dominant orientation. Conversely, cells did not show any preferred orientation on unstretched samples. The HA and fiber alignment both improved cell proliferation after 72 hours with the stretched HA modified samples having the highest level of cell proliferation among all samples. Results of FFT and circularity analysis revealed that actin orientation and nuclei elongation were directly influenced by surface morphology. This work not only introduces a substrate that induces cell alignment through surface orientation, but it also shows the high impact of HA on cell proliferation even at low percentage of 10%. Considering the hierarchical structure of bone with the HA being the main mineral present in its structure, oriented matrix is a crucial prerequisite for bone regeneration. Our results are particularly beneficial for bone tissue engineering where a highly aligned ECM structure in presence of HA is crucial[96].

CHAPTER 5

CONCLUSION AND RECOMMENDATIONS

In **chapter 2**, an engineering solution to reduce the size of synthetic hydroxyapatite was suggested. A simple hydrothermal method presented by Liu et al was modified to develop an in-situ one step synthesis method capable of efficiently producing large quantities of biologically relevant HA suitable for use in biological applications. An in-situ milling process resulted in smaller particle size and this simple method avoids the need for continuous monitoring of pH and temperature that is prevalent in other HA synthesis approaches. Then, the lack of bioactive ECM mimic structures for bone regeneration established the motivation to create aligned CNF/HA composites by applying external force in **chapter 3**. The correlation between applied force and fiber orientation was explored and optimum force for maximized alignment was quantified. It was demonstrated that HA modified films had the same level of fiber orientation compared to pure CNF films. In **chapter 4**, biological assays were performed to evaluate films cytotoxicity and cellular alignment. The results revealed that HA remarkably improves cell proliferation and simultaneous presence of HA and orientation led to the highest level of cell proliferation. MC3T3E1 cell morphology experiments showed substantial cytoskeleton alignment and nuclei elongation on stretched substrates.

Although HA nanoparticles significantly increased cell proliferation, however, it caused a decrease in tensile strength when compared to pure CNF. Hydroxyapatite nanoparticles create spaces between the cellulose fibrils and at higher percentage this can drastically decrease tensile properties. One possible solution to address this limitation is to take advantage of additives such as polyethylene glycol (PEG) to improve hydrogen bonding among fibers. PEG will bring fibers closer together by hydrogen bonding and can possibly improve tensile strength. One interesting aspect that future studies can focus on, is to

evaluate biochemical changes occurring on the surface of films due to metabolic activities and their effect on mechanical properties of the films at different time points.

REFERENCES

1.   Amini, A.R., C.T. Laurencin, and S.P. Nukavarapu, *Bone tissue engineering: recent advances and challenges.* Critical Reviews™ in Biomedical Engineering, 2012. **40**(5).

2.   Ho-Shui-Ling, A., et al., *Bone regeneration strategies: Engineered scaffolds, bioactive molecules and stem cells current stage and future perspectives.* Biomaterials, 2018. **180**: p. 143-162.

3.   Fillingham, Y. and J. Jacobs, *Bone grafts and their substitutes.* The bone & joint journal, 2016. **98-B**(1 Suppl A): p. 6.

4.   Morris, M.T., S.P. Tarpada, and W. Cho, *Bone graft materials for posterolateral fusion made simple: a systematic review.* European Spine Journal, 2018. **27**(8): p. 1856-1867.

5.   Wang, W. and K.W.K. Yeung, *Bone grafts and biomaterials substitutes for bone defect repair: A review.* Bioactive materials, 2017. **2**(4): p. 224-247.

6.   Hollister, S.J. and W.L. Murphy, *Scaffold translation: barriers between concept and clinic.* Tissue Engineering Part B: Reviews, 2011. **17**(6): p. 459-474.

7.   Bara, J.J., et al., *Improving translation success of cell-based therapies in orthopaedics.* Journal of Orthopaedic Research, 2016. **34**(1): p. 17-21.

8.   Nicolas, J., et al., *3D Extracellular Matrix Mimics: Fundamental Concepts and Role of Materials Chemistry to Influence Stem Cell Fate.* Biomacromolecules, 2020. **21**(6): p. 1968-1994.

9.   Hunter, N.L. and R.E. Sherman, *Combination products: modernizing the regulatory paradigm.* Nature Reviews Drug Discovery, 2017. **16**(8): p. 513-514.

10.   Burdick, J.A., et al., *Acellular biomaterials: an evolving alternative to cell-based therapies.* Science translational medicine, 2013. **5**(176): p. 176ps4-176ps4.

11.   Wang, S., et al., *Mineralized collagen-based composite bone materials for cranial bone regeneration in developing sheep.* ACS Biomaterials Science & Engineering, 2017. **3**(6): p. 1092-1099.

12.   Koons, G.L., M. Diba, and A.G. Mikos, *Materials design for bone-tissue engineering.* Nature Reviews Materials, 2020. **5**(8): p. 584-603.

13.   Chen, S., et al., *Biomaterials with structural hierarchy and controlled 3D nanotopography guide endogenous bone regeneration.* Science Advances, 2021. **7**(31): p. eabg3089.

14.   He, M., et al., *Hierarchically multi-functionalized graded membrane with enhanced bone regeneration and self-defensive antibacterial characteristics for guided bone regeneration.* Chemical Engineering Journal, 2020. **398**: p. 125542.

15.   Jose, M.V., et al., *Aligned PLGA/HA nanofibrous nanocomposite scaffolds for bone tissue engineering.* Acta biomaterialia, 2009. **5**(1): p. 305-315.

16.   Olvera, D., et al., *Modulating microfibrillar alignment and growth factor stimulation to regulate mesenchymal stem cell differentiation.* Acta biomaterialia, 2017. **64**: p. 148-160.

17.   Xie, J., et al., *Radially aligned, electrospun nanofibers as dural substitutes for wound closure and tissue regeneration applications.* ACS nano, 2010. **4**(9): p. 5027-5036.

18.   Trache, D., et al., *Nanocellulose: From Fundamentals to Advanced Applications.* Frontiers in Chemistry, 2020. **8**(392).

19.   Liu, F., et al., *Nanocellulose-Reinforced Hydroxyapatite Nanobelt Membrane as a Stem Cell Multi-Lineage Differentiation Platform for Biomimetic Construction of Bioactive 3D Osteoid Tissue In Vitro.* Advanced healthcare materials, 2021. **10**(8): p. e2001851.

20.   Glimcher, M.J., *Bone; nature of the calcium phosphate crystals and cellular, structural, and physical chemical mechanisms in their formation.* Reviews in mineralogy and geochemistry, 2006. **64**(1): p. 223-282.

21.   Grandfield, K., V. Vuong, and H.P. Schwarcz, *Ultrastructure of Bone: Hierarchical Features from Nanometer to Micrometer Scale Revealed in Focused Ion Beam Sections in the TEM.* Calcified tissue international, 2018. **103**(6): p. 606-616.

22.   Reznikov, N., et al., *Fractal-like hierarchical organization of bone begins at the nanoscale.* Science (American Association for the Advancement of Science), 2018. **360**(6388).

23.   Wopenka, B. and J.D. Pasteris, *A mineralogical perspective on the apatite in bone.* Materials Science & Engineering C, 2005. **25**(2): p. 131-143.

24.   Von Euw, S., et al., *Bone mineral: new insights into its chemical composition.* Scientific reports, 2019. **9**(1): p. 8456-8456.

25.   Vanderby, R. and P.P. Provenzano, *Collagen in connective tissue: from tendon to bone.* Journal of Biomechanics, 2003. **36**(10): p. 1523-1527.

26.   Ceballos, D., et al., *Magnetically Aligned Collagen Gel Filling a Collagen Nerve Guide Improves Peripheral Nerve Regeneration.* Experimental Neurology, 1999. **158**(2): p. 290-300.

27.   Gao, C., et al., *Bone biomaterials and interactions with stem cells.* Bone Research, 2017. **5**(1): p. 17059.

28.   Dimitriou, R., et al., *Bone regeneration: current concepts and future directions.* BMC medicine, 2011. **9**(1): p. 66-66.

29.   Einhorn, T.A. and L.C. Gerstenfeld, *Fracture healing: mechanisms and interventions.* Nature reviews. Rheumatology, 2015. **11**(1): p. 45-54.

30.   Ferguson, C., et al., *Does adult fracture repair recapitulate embryonic skeletal formation?* Mechanisms of development, 1999. **87**(1): p. 57-66.

31.   Harwood, P.J. and D.O. Ferguson, *(ii) An update on fracture healing and non-union.* Orthopaedics and trauma, 2015. **29**(4): p. 228-242.

32.   Schlickewei, C.W., et al., *Current and future concepts for the treatment of impaired fracture healing.* International journal of molecular sciences, 2019. **20**(22): p. 5805.

33.   Bahney, C.S., et al., *Cellular biology of fracture healing.* Journal of Orthopaedic Research®, 2019. **37**(1): p. 35-50.

34.   Audigé, L., et al., *Path analysis of factors for delayed healing and nonunion in 416 operatively treated tibial shaft fractures.* Clinical orthopaedics and related research, 2005. **438**: p. 221.

35.   Giannoudis, P.V., T.A. Einhorn, and D. Marsh, *Fracture healing: The diamond concept.* Injury, 2007. **38**: p. S3-S6.

36.   Jimi, E., et al., *The Current and Future Therapies of Bone Regeneration to Repair Bone Defects.* International journal of dentistry, 2012. **2012**: p. 148261-7.

37.   Hak, D., *Bone Grafting and Bone Graft Substitutes.*

38.   Campana, V., et al., *Bone substitutes in orthopaedic surgery: from basic science to clinical practice.* Journal of materials science. Materials in medicine, 2014. **25**(10): p. 2445-2461.

39.   Giannoudis, P.V., H. Dinopoulos, and E. Tsiridis, *Bone substitutes: An update.* Injury, 2005. **36**(3): p. S20-S27.

40.   Armiento, A.R., et al., *Functional biomaterials for bone regeneration: a lesson in complex biology.* Advanced Functional Materials, 2020. **30**(44): p. 1909874.

41.   Kim, M., et al., *Biomimetic cellulose/calcium-deficient-hydroxyapatite composite scaffolds fabricated using an electric field for bone tissue engineering.* RSC advances, 2018. **8**(37): p. 20637-20647.

42.   Kim, D.-H., et al., *Matrix nanotopography as a regulator of cell function.* The Journal of cell biology, 2012. **197**(3): p. 351-360.

43.   Du, H., et al., *Cellulose nanocrystals and cellulose nanofibrils based hydrogels for biomedical applications.* Carbohydrate polymers, 2019. **209**: p. 130-144.

44.   Alexandrescu, L., et al., *Cytotoxicity tests of cellulose nanofibril-based structures.* Cellulose, 2013. **20**(4): p. 1765-1775.

45.   Manhas, N., et al., *PCL/PVA nanoencapsulated reinforcing fillers of steam exploded/autoclaved cellulose nanofibrils for tissue engineering applications.* RSC advances, 2015. **5**(31): p. 23999-24008.

46.   Hench, L.L. and I. Thompson, *Twenty-first century challenges for biomaterials.* Journal of the Royal Society interface, 2010. **7**(Suppl-4): p. S379-S391.

47.   Holzwarth, J.M. and P.X. Ma, *Biomimetic nanofibrous scaffolds for bone tissue engineering.* Biomaterials, 2011. **32**(36): p. 9622-9629.

48.   Ana, I.D., S. Matsuya, and K. Ishikawa, *Engineering of carbonate apatite bone substitute based on composition-transformation of gypsum and calcium hydroxide.* Engineering, 2010. **2**(05): p. 344.

49.   Clarke, B., *Normal Bone Anatomy and Physiology.* Clinical journal of the American Society of Nephrology, 2008. **3**(Supplement 3): p. S131-S139.

50.   Geng, Z., et al., *Synthesis, Characterization, and Biological Evaluation of Nanostructured Hydroxyapatite with Different Dimensions.* Nanomaterials (Basel, Switzerland), 2017. **7**(2): p. 38.

51.   Zakaria, S.M., et al., *Nanophase hydroxyapatite as a biomaterial in advanced hard tissue engineering: a review.* Tissue Engineering Part B: Reviews, 2013. **19**(5): p. 431-441.

52.   Geng, Y., et al., *Clock-pump four-wave-mixing-based multichannel all-optical regeneration in silicon waveguide.* Optical Engineering, 2017. **56**(11): p. 117102.

53.   Fathi, M., A. Hanifi, and V. Mortazavi, *Preparation and bioactivity evaluation of bone-like hydroxyapatite nanopowder.* Journal of materials processing technology, 2008. **202**(1-3): p. 536-542.

54.   Boutinguiza, M., et al., *Biological hydroxyapatite obtained from fish bones.* Materials Science and Engineering: C, 2012. **32**(3): p. 478-486.

55.   Lee, S.W., et al., *Comparative study of hydroxyapatite prepared from seashells and eggshells as a bone graft material*. 2014.

56.   Johnson, G.S., M.R. Mucalo, and M.A. Lorier, *The processing and characterization of animal-derived bone to yield materials with biomedical applications Part 1: Modifiable porous implants from bovine condyle cancellous bone and characterization of bone materials as a function of processing.* Journal of materials science. Materials in medicine, 2000. **11**(7): p. 427-441.

57.   Tan, L., et al., *Biodegradable Materials for Bone Repairs: A Review.* Journal of Materials Science & Technology, 2013. **29**(6): p. 503-513.

58.   Ratnayake, J.T., et al., *Development and characterization of a xenograft material from N ew Z ealand sourced bovine cancellous bone.* Journal of Biomedical Materials Research Part B: Applied Biomaterials, 2017. **105**(5): p. 1054-1062.

59.   Suchanek, W.L., et al., *Mechanochemical–hydrothermal synthesis of carbonated apatite powders at room temperature.* Biomaterials, 2002. **23**(3): p. 699-710.

60.   Scuderi, G.R. and A.J. Tria, *Knee arthroplasty handbook: techniques in total knee and revision arthroplasty*. 2006: Springer Science & Business Media.

61.   Tang, Z., et al., *The material and biological characteristics of osteoinductive calcium phosphate ceramics.* Regenerative biomaterials, 2018. **5**(1): p. 43-59.

62.   Liu, H.S., et al., *Hydroxyapatite synthesized by a simplified hydrothermal method.* Ceramics International, 1997. **23**(1): p. 19-25.

63.   Kong, L.B., J. Ma, and F. Boey, *Nanosized hydroxyapatite powders derived from coprecipitation process.* Journal of materials science, 2002. **37**(6): p. 1131-1134.

64.   Fathi, M.H. and A. Hanifi, *Evaluation and characterization of nanostructure hydroxyapatite powder prepared by simple sol–gel method.* Materials Letters, 2007. **61**(18): p. 3978-3983.

65.   Sadat-Shojai, M., M.-T. Khorasani, and A. Jamshidi, *Hydrothermal processing of hydroxyapatite nanoparticles—A Taguchi experimental design approach.* Journal of Crystal Growth, 2012. **361**: p. 73-84.

66.   Han, Y.J., et al., *Investigation of the bioactivity and biocompatibility of different glass interfaces with hydroxyapatite, fluorohydroxyapatite and 58S bioactive glass.* Biofactors, 2007. **30**(4): p. 205-216.

67.   Yeong, K.C.B., J. Wang, and S.C. Ng, *Mechanochemical synthesis of nanocrystalline hydroxyapatite from CaO and CaHPO4.* Biomaterials, 2001. **22**(20): p. 2705-2712.

68.   Dorozhkin, S.V., *Calcium orthophosphate-based biocomposites and hybrid biomaterials.* Journal of Materials Science, 2009. **44**(9): p. 2343-2387.

69.   Chen, X.B., N. Birbilis, and T.B. Abbott, *A simple route towards a hydroxyapatite–Mg(OH)2 conversion coating for magnesium.* Corrosion Science, 2011. **53**(6): p. 2263-2268.

70.   Poinern, G.J.E., et al., *Thermal and ultrasonic influence in the formation of nanometer scale hydroxyapatite bio-ceramic.* International journal of nanomedicine, 2011. **6**: p. 2083-2095.

71.   Liu, Q., et al., *Insight into biological apatite: physiochemical properties and preparation approaches.* BioMed research international, 2013. **2013**.

72.   Giraldo-Betancur, A.L., et al., *Comparison of physicochemical properties of bio and commercial hydroxyapatite.* Current Applied Physics, 2013. **13**(7): p. 1383-1390.

73.   Malina, D., K. Biernat, and A. Sobczak-Kupiec, *Studies on sintering process of synthetic hydroxyapatite.* Acta biochimica Polonica, 2013. **60**(4): p. 851.

74.   Barinov, S., et al., *Carbonate release from carbonated hydroxyapatite in the wide temperature rage.* Journal of Materials Science: Materials in Medicine, 2006. **17**(7): p. 597-604.

75.   Supardi, A., Z.I. Nisa, and D. Hikmawati, *Synthesis of nanohydroxyapatite from cuttlefish bone (Sepia sp.) using milling method.* International journal of biomaterials, 2019. **2019**.

76.   Khalil, H., et al., *A review on micro-to nanocellulose biopolymer scaffold forming for tissue engineering applications.* Polymers, 2020. **12**(9): p. 2043.

77.   Pennells, J., et al., *Trends in the production of cellulose nanofibers from non-wood sources.* Cellulose (London), 2019. **27**(2): p. 575-593.

78. Wahlström, N., et al., *Cellulose from the green macroalgae Ulva lactuca: isolation, characterization, optotracing, and production of cellulose nanofibrils.* Cellulose (London), 2020. **27**(7): p. 3707-3725.

79. Luo, H., et al., *Advances in tissue engineering of nanocellulose-based scaffolds: A review.* Carbohydrate polymers, 2019. **224**: p. 115144-115144.

80. Zhang, K., et al., *Cellulose Nanofibers: Fabrication and Surface Functionalization Techniques*, in *Handbook of Nanofibers*, A. Barhoum, M. Bechelany, and A.S.H. Makhlouf, Editors. 2019, Springer International Publishing: Cham. p. 409-449.

81. Ye, D., et al., *Preferred crystallographic orientation of cellulose in plant primary cell walls.* Nature communications, 2020. **11**(1): p. 4720-4720.

82. Moohan, J., et al., *Cellulose Nanofibers and Other Biopolymers for Biomedical Applications. A Review.* Applied sciences, 2019. **10**(1): p. 65.

83. Seddiqi, H., et al., *Cellulose and its derivatives: towards biomedical applications.* Cellulose (London), 2021. **28**(4): p. 1893-1931.

84. Bacakova, L., et al., *Versatile Application of Nanocellulose: From Industry to Skin Tissue Engineering and Wound Healing.* Nanomaterials (Basel, Switzerland), 2019. **9**(2): p. 164.

85. Hasan, N., et al., *Recent advances of nanocellulose in drug delivery systems.* Journal of pharmaceutical investigation, 2020. **50**(6): p. 553-572.

86. Park, M., et al., *Effect of negatively charged cellulose nanofibers on the dispersion of hydroxyapatite nanoparticles for scaffolds in bone tissue engineering.* Colloids and surfaces, B, Biointerfaces, 2015. **130**: p. 222-228.

87. Sofi, H.S., et al., *Regenerated cellulose nanofibers from cellulose acetate: Incorporating hydroxyapatite nanoparticles , as a scaffold for tissue engineering applications.* Materials Science & Engineering C, 2021. **118**.

88. Salama, A., et al., *Soy protein hydrolysate grafted cellulose nanofibrils with bioactive signals for bone repair and regeneration.* Carbohydrate polymers, 2020. **229**: p. 115472-115472.

89. Abouzeid, R.E., et al., *Biomimetic Mineralization of Three-Dimensional Printed Alginate/TEMPO-Oxidized Cellulose Nanofibril Scaffolds for Bone Tissue Engineering.* Biomacromolecules, 2018. **19**(11): p. 4442-4452.

90. Li, K., et al., *Alignment of Cellulose Nanofibers: Harnessing Nanoscale Properties to Macroscale Benefits.* ACS nano, 2021. **15**(3): p. 3646-3673.

91. He, X., et al., *Uniaxially Aligned Electrospun All-Cellulose Nanocomposite Nanofibers Reinforced with Cellulose Nanocrystals: Scaffold for Tissue Engineering.* Biomacromolecules, 2014. **15**(2): p. 618-627.

92.   Badylak, S.F., D.O. Freytes, and T.W. Gilbert, *Extracellular matrix as a biological scaffold material: Structure and function.* Acta biomaterialia, 2009. **5**(1): p. 1-13.

93.   Zheng, Y., et al., *Bio-inspired composite by hydroxyapatite mineralization on (bis) phosphonate-modified cellulose-alginate scaffold for bone tissue engineering.* Colloids and Surfaces A: Physicochemical and Engineering Aspects, 2021: p. 127958.

94.   Chesley, M., et al., *One-step hydrothermal synthesis with in situ milling of biologically relevant hydroxyapatite.* Materials Science & Engineering C, 2020. **113**: p. 110962-110962.

95.   Siddiqui, H.A., K.L. Pickering, and M.R. Mucalo, *A Review on the Use of Hydroxyapatite-Carbonaceous Structure Composites in Bone Replacement Materials for Strengthening Purposes.* Materials, 2018. **11**(10): p. 1813.

96.   Liao, S., C.K. Chan, and S. Ramakrishna, *Stem cells and biomimetic materials strategies for tissue engineering.* Materials Science and Engineering: C, 2008. **28**(8): p. 1189-1202.

97.   Nazari, B. and D.W. Bousfield, *Cellulose nanofibers influence on properties and processing of paperboard coatings.* Nordic pulp & paper research, 2016. **31**(3): p. 511-520.

98.   Montana, G., *Ceramic raw materials: how to recognize them and locate the supply basins—mineralogy, petrography.* Archaeological and anthropological sciences, 2020. **12**(8).

99.   Püspöki, Z., et al., *Transforms and Operators for Directional Bioimage Analysis: A Survey.* Advances in anatomy, embryology and cell biology, 2016. **219**: p. 69.

100.   Ghasemi, S., et al., *Birefringence-based orientation mapping of cellulose nanofibrils in thin films.* Cellulose (London), 2019. **27**(2): p. 677-692.

101.   Wei, Z., et al., *Nanocellulose based hydrogel or aerogel scaffolds for tissue engineering.* Cellulose, 2021. **28**(12): p. 7497-7520.

102.   Pal, V.K., et al., *Designing nanofibrillar cellulose peptide conjugated polymeric hydrogel scaffold for controlling cellular behaviour.* Cellulose, 2021. **28**(16): p. 10335-10357.

103.   Weiner, S. and H.D. Wagner, *The material bone: structure-mechanical function relations.* Annual review of materials science, 1998. **28**(1): p. 271-298.

104.   Nakano, T., et al., *Unique alignment and texture of biological apatite crystallites in typical calcified tissues analyzed by microbeam X-ray diffractometer system.* Bone, 2002. **31**(4): p. 479-487.

105.   Sekita, A., et al., *Synchronous disruption of anisotropic arrangement of the osteocyte network and collagen/apatite in melanoma bone metastasis.* Journal of structural biology, 2017. **197**(3): p. 260-270.

106.   Ozasa, R., et al., *Construction of human induced pluripotent stem cell-derived oriented bone matrix microstructure by using in vitro engineered anisotropic culture model.* Journal of Biomedical Materials Research Part A, 2018. **106**(2): p. 360-369.

107.	Zhou, H. and J. Lee, *Nanoscale hydroxyapatite particles for bone tissue engineering.* Acta biomaterialia, 2011. **7**(7): p. 2769-2781.

108.	Chae, T., et al., *Novel biomimetic hydroxyapatite/alginate nanocomposite fibrous scaffolds for bone tissue regeneration.* Journal of Materials Science: Materials in Medicine, 2013. **24**(8): p. 1885-1894.

109.	Martínez-Vázquez, F., et al., *Fabrication of novel Si-doped hydroxyapatite/gelatine scaffolds by rapid prototyping for drug delivery and bone regeneration.* Acta biomaterialia, 2015. **15**: p. 200-209.

110.	Morimune-Moriya, S., et al., *Hydroxyapatite formation on oxidized cellulose nanofibers in a solution mimicking body fluid.* Polymer Journal, 2015. **47**(2): p. 158-163.

111.	Guo, Y.-P., et al., *Hybrid nanostructured hydroxyapatite–chitosan composite scaffold: bioinspired fabrication, mechanical properties and biological properties.* Journal of Materials Chemistry B, 2015. **3**(23): p. 4679-4689.

112.	Zimmermann, K.A., et al., *Biomimetic design of a bacterial cellulose/hydroxyapatite nanocomposite for bone healing applications.* Materials Science and Engineering: C, 2011. **31**(1): p. 43-49.

113.	Luo, Y., et al., *Concentrated gelatin/alginate composites for fabrication of predesigned scaffolds with a favorable cell response by 3D plotting.* RSC Advances, 2015. **5**(54): p. 43480-43488.

114.	Taylor, S.E., et al., *Objective Morphological Quantification of Microscopic Images Using a Fast Fourier Transform (FFT) Analysis.* Current protocols essential laboratory techniques, 2013. **95**(Suppl 7): p. 9.5.1.

115.	Li, X., et al., *Effects of aligned and random fibers with different diameter on cell behaviors.* Colloids and Surfaces B: Biointerfaces, 2018. **171**: p. 461-467.

BIOGRAPHY OF THE AUTHOR

Sahar earned her Master's degree in Biomedical Engineering from the University of Tehran in 2017 and immediately started her PhD in Biomedical Engineering. Sahar was awarded the best poster presentation award as a PhD candidate in 2021. Sahar is a candidate for the Doctor of Philosophy degree in Biomedical Engineering from the University of Maine in May 2022.